CHALMERS
UNIVERSITY OF TECHNOLOGY

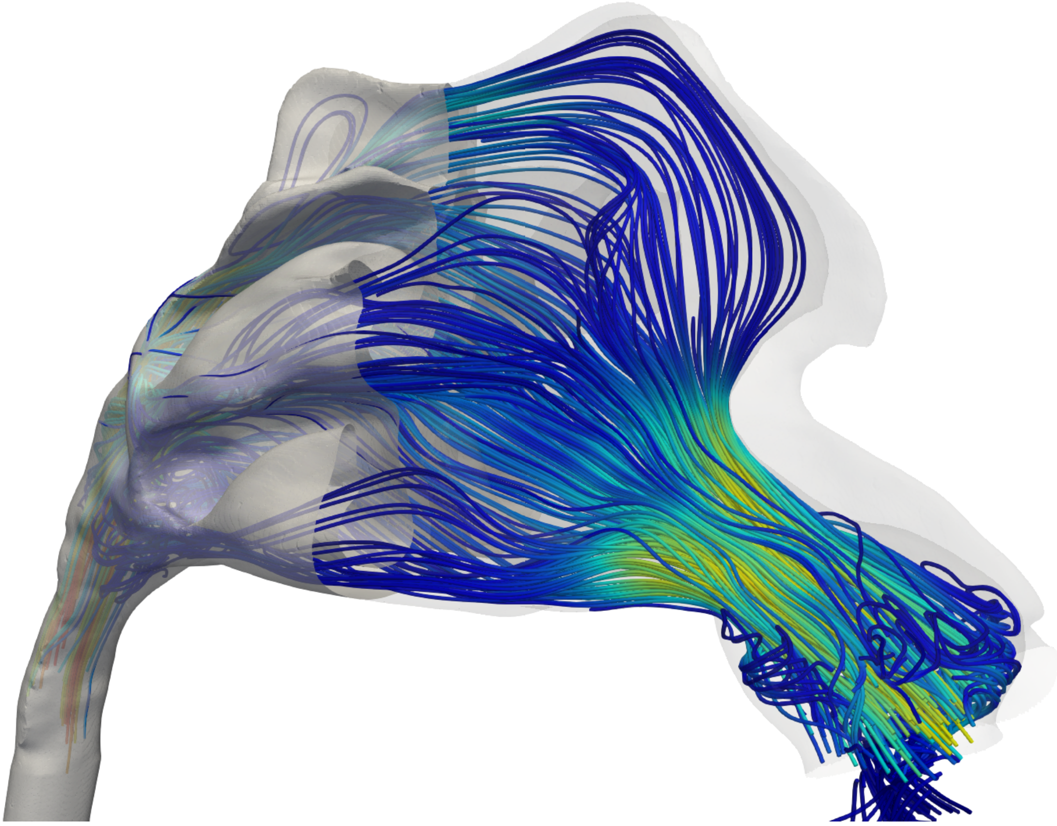

Computational modeling of airflow in a human nasal cavity

Master's thesis in Applied Mechanics

AMEY RAJU PAWADE

DEPARTMENT OF MECHANICS AND MARITIME SCIENCES

CHALMERS UNIVERSITY OF TECHNOLOGY
Gothenburg, Sweden 2021
www.chalmers.se

Master's thesis 2021

Computational modeling of airflow in a human nasal cavity

AMEY RAJU PAWADE

Department of Mechanics and Maritime Sciences
Division of Fluid Dynamics
Chalmers University of Technology
Gothenburg, Sweden 2021

Computational modeling of airflow in a human nasal cavity
AMEY RAJU PAWADE

Supervisor: Håkan Nilsson, Department of Mechanics and Maritime Sciences
Valery Chernoray, Department of Mechanics and Maritime Sciences
Ebrahim Ghahramani, Department of Mechanics and Maritime Sciences
Torbjörn Lundh, Department of Mathematical Sciences
Johan Hellgren, Sahlgrenska University Hospital
Examiner: Håkan Nilsson, Department of Mechanics and Maritime Sciences

Master's Thesis 2021:66
Department of Mechanics and Maritime Sciences
Division of Fluid Dynamics
Chalmers University of Technology
SE-412 96 Gothenburg
Telephone +46 31 772 1000

Cover: Visualization of streamlines in the nasal cavity model 2.

Typeset in LaTeX
Gothenburg, Sweden 2021

Computational modeling of airflow in a human nasal cavity
AMEY RAJU PAWADE
Department of Mechanics and Maritime Sciences
Chalmers University of Technology

Abstract

Nasal obstructions restrict the flow of air through the nasal passage, and a failure to accurately identify these obstructions can lead to long-term discomfort in the patients. There is a need to develop new methods to diagnose nasal obstructions because the current subjective and objective methods do not always strongly correlate, resulting in the medical and surgical procedures being sub-optimal and thus reducing patient comfort. The advancement in computing and imaging technology enables the application of novel methods like Computational Fluid Dynamics (CFD) and 3D imaging to diagnose nasal obstructions.

This project aims to understand the effect of tidal breathing in the nasal cavity and investigate the possibility of using CFD as a tool in diagnosing nasal obstructions. In-vitro experiments were performed on the 3D-printed model of the nasal cavity to evaluate the nasal resistance and pressure distribution inside the nasal passage. The approach of modeling the nasal cavity flow by a quasi-steady assumption was analyzed by comparing the steady-state solution with results from tidal breathing simulation.

The in-vitro pressure distribution and nasal resistance were similar to the results obtained from tidal breathing CFD simulations. It validates the CFD methodology established in this project and indicates that CFD as a tool can be used as an objective method to diagnose nasal obstructions. Although the nasal resistance is accurately calculated from the steady-state solution, the flow characteristics during the exhalation differ significantly compared to tidal breathing simulations. It highlights that the quasi-steady assumption is inappropriate to study the detailed flow structures inside the nasal cavity.

The conclusions derived from this project suggest that the post-processing capabilities of CFD can aid doctors in acquiring valuable insights regarding nasal airflow. In the future, CFD simulations can help understand the effect of various surgical procedures by performing virtual surgery on the obstructed cavity of the patient.

Keywords: Nasal cavity, nasal resistance, rhinomanometry, tidal breathing, CFD

Acknowledgements

First and foremost, I am extremely grateful to all the supervisors involved in this project - Håkan Nilsson, Valery Chernoray, Johan Hellgren, Torbjörn Lundh, and Ebrahim Ghahramani. I have greatly benefited from their expertise in the field of medical sciences and fluid mechanics. It helped me create a concrete plan of action, set reasonable goals, and eventually achieve the objectives of this project. The constant feedback and support provided by them certainly proved monumental towards the success of this inter-disciplinary project.

I would like to recognize the invaluable assistance provided by Jesper Buske and Gulliver Koch. They have persistently helped me during various phases of this project - creating the 3D model of the cavity, setting up the experimental rig, and performing the experiments. Besides that, the resources provided by Chalmers Centre for Computational Science and Engineering (C3SE) on Hebbe and Vera PC clusters proved very useful in reducing the computational time for the simulations.

I would also like to thank all my friends, for encouraging and supporting me whenever I needed them. Most importantly, I am grateful for my family's unconditional, unequivocal, and loving support.

Amey Raju Pawade, Gothenburg, August 2021

Contents

List of Figures

List of Tables

1

Introduction

1.1 Background

One of the common problems observed by Ear, Nose, and Throat (ENT) specialists is nasal obstruction. The etiology of nasal obstruction can generally be divided into two categories - inflammatory or structural. Structural nasal obstruction is a result of septal deviation, nasal polyps, or other anatomical anomalies, while inflammatory nasal obstruction is a consequence of swelling of nasal mucosa due to infection, allergic or non-allergic rhinitis [1]. Nasal obstructions cause a huge discomfort to the respiratory system and can lead to sleeping disorders, snoring, and Obstructive Sleep Apnea (OSA). Hence, precise diagnosis and treatment of nasal obstruction are of utmost importance.

Nasal obstruction caused by inflammation can be easily diagnosed with a decongestant spray, however, for structural nasal obstructions, surgeries such as septoplasty and turbinectomy are most commonly performed in the field of otolaryngology. For these surgeries, the clinician typically relies on various subjective and objective methods to assess the nasal obstruction in patients. Rhinomanometry is a commonly used objective method and is considered today's gold standard. However, the nasal obstruction evaluated using objective measurements does not always correlate strongly with the patient's reported feeling of patency [2]. This results in surgical and medical procedures being sub-optimal which reduces patient satisfaction, long-term health benefits, and health economics. In the National Swedish Register for Septoplasty, 25% of the patients are not satisfied with the result. Furthermore, some articles report a failure rate of 20-50% for surgeries related to nasal obstructions [3].

Due to the advances in computer, imaging, and bioengineering technology, clinicians can get a measure of nasal obstruction using novel objective methods like 3D Imaging and Computational Fluid Dynamics (CFD) [4]. CFD is a branch of fluid mechanics that uses various numerical analysis techniques to solve the partial differential Navier-Stokes equations that govern the motion of the fluid. Thus, a 3D model of a patient's nasal cavity can be reconstructed for a better understanding of the anatomy of the patient's nose, whereas CFD tools can be utilized to obtain information about the flow variables like velocity, pressure, wall shear stress, turbulence, and flow distribution in various regions of the nasal cavity, something which is not possible using other objective methods like rhinomanometry or anterior rhinomanometry.

Furthermore, improving on these techniques, the nasal cavity of a patient can be digitally modified through various modeling tools, thus undergoing a virtual surgery. The doctor can then use CFD analysis to study the airflow in the modified nasal cavity and understand the effect of various surgical interventions. It will aid in an accurate diagnosis and treatment for the patient. This approach can enable better patient management by providing additional information in diagnosing patients with nasal obstruction [5].

However, CFD has its pitfalls, as the underlying physics is complex, and the results generated by CFD are at best as good as the physics embedded in it and at worst as good as the operator [6]. The results depend on the discretization of the region of interest, the choice of initial and boundary conditions, and a suitable numerical method. Consequently, it is essential to validate the CFD results with the results from the current tools used by the doctors to diagnose nasal obstruction.

The project is a continuation of a previous thesis by Ronnås and Widebrant, who explored the possibilities of using CFD simulations in the diagnosis and treatment of nasal obstruction by recreating the rhinomanometry curves [7]. The current study focuses on understanding the flow dynamics in the nasal cavity during the tidal breathing condition (inhalation and exhalation during restful breathing). Additionally, CFD results are validated using rhinomanometry and pressure measurement experiments.

1.2 Literature survey

Cherobin *et al.* investigated the correlation and agreement between the nasal resistances derived from CFD (R_{CFD}) and rhinomanometry (R_{RMN}). The authors reported a weak correlation between CFD and rhinomanometry-derived nasal resistance. However, R_{CFD} was calculated by performing a steady-state simulation, and the value was based on the classical method at a reference pressure of 75 Pa, whereas R_{RMN} results were based on actual human tidal breathing. The authors suggested that the correlation can be improved by comparing nasal resistance derived from unsteady CFD simulation and rhinomanometry [8].

A study from Radulesco *et al.* involving patients with septal deviation reported that nasal resistance derived from CFD and rhinomanometry had strong correlations with patient's perception of nasal airflow. However, when comparing the unilateral nasal resistance from CFD and rhinomanometry, a statistically significant difference was observed [9]. Zhao *et al.* observed a statistically significant but weak correlation between CFD and rhinomanometry nasal resistance. To improve the objective methods for diagnosis of nasal obstruction, they recommend combining several objective variables like nasal heat loss, nasal trigeminal sensitivity, and nasal resistance for future studies in this area [10].

Wong and Eccles performed rhinomanometry using the Classical and Broms method on four model noses to compare the unilateral Nasal Airway Resistance (NAR) [11]. The study concluded that at low resistances, NAR measured by Broms method is similar to the Classical method at 75 Pa, but is significantly different from measurements obtained using the Classical method at 150 Pa. At high resistances, similar NAR values were seen for Broms and Classical method at 150 Pa, whereas for Broms and Classical method at 75 Pa, the measurements showed significant differences. The authors deduced that the choice of method used to analyze the pressure-flow curve could alter the perception of the doctor in evaluating the nasal resistance in patients.

Time-dependent characteristics of flow using large-eddy simulations (LES) was studied by Lee *et al.* A significant difference in flow characteristics during the exhalation phase was observed when comparing the steady-state simulations and unsteady simulations. Based on this observation, the authors highlighted the importance of inertial effects, caused as a result of the variation in mass flux of air [12]. Several research papers evaluate the effect of unsteady cyclic airflow in the nasal cavity, but the nasal resistance calculated using CFD and rhinomanometry have not been compared in these studies [13, 14].

Moreddu *et al.* evaluated the nasal resistance using dynamic pressure-flow curves obtained by performing unsteady CFD simulations and described a methodology of numerical rhinomanometry. The authors reported a good agreement between CFD and rhinomanometry-based nasal resistance and encouraged that with increased computing power in the future, CFD as a tool could be significant in surgical decision-making and prediction of surgical results [15].

1.3 Project aim

As seen in the literature study, there are a few studies concerning the effect of tidal breathing on the flow field in the nasal cavity. The project aims to better understand the effect of tidal breathing in the nasal cavity and explore the prospects of CFD in the diagnosis of nasal obstructions by comparing the tidal breathing simulations results with in-vitro rhinomanometry experiments. The project aim is further divided into tasks as specified below.

- To obtain an anatomically accurate representation of the nasal cavity from Computed Tomography (CT) scan to generate a computational mesh and a 3D model.
- To design and build a rig representing an 'artificial lung' for driving the flow in the nasal cavity, thus mimicking a human tidal breath.
- To validate the CFD results by measuring and comparing the pressure drop at various probes in the nasal cavity during experiments.
- To compare nasal resistance obtained from in-vitro rhinomanometry experi-

ments with the CFD-derived nasal resistance.

- To compare the flow-field and CFD-derived nasal resistance from tidal breathing simulation with the transient constant flowrate simulation.

1.4 Delimitations

The main region of interest in this study was the nasal cavity, and thus the final geometry obtained from the CT scan consisted of the nasal cavity extending from the nostrils to the larynx. The paranasal sinuses were excluded in the segmentation process, and the corresponding Ostia were closed to make an air-tight geometry. The walls of the nasal cavity are assumed to be rigid and no movement is incorporated.

The actual inhalation and exhalation process of a human in resting condition is periodic, with the exhalation cycle being a bit longer in duration. However, in this project, the breathing cycle is considered to be an approximate sinusoidal curve. It ensures that a similar breathing pattern is provided as a boundary condition to the CFD simulation and the in-vitro experiments.

For a medical study, a comparison involving a large cohort is preferred for statistical correctness. Due to the cost and time involved in generating the 3D model from a CT scan, only two nasal cavities are considered for this project to compare the nasal resistance calculated from the CFD result and the in-vitro rhinomanometry experiment.

1.5 Ethical considerations

The project could prove important in understanding the airflow inside a nasal cavity during tidal breathing. The methods and results from the project could be of value for further research in this area. However, the results presented in the study should carefully be analyzed considering the limitations as stated earlier.

The CT scan data provided by Sahlgrenska university was used to generate a 3D model of the nasal cavity for simulations and experiments. These CT scans are anonymous to protect the privacy of the individual. Moreover, to ensure anonymity, alterations were made to the facial surface before using it further. The nasal model provided by Strien *et al.* [16] in their research paper was also used in this project. With the permission of the corresponding authors, the data was used to reproduce a computerized mesh and a 3D model.

2

Theory

2.1 Upper respiratory tract of humans

To comprehend the results generated from the CFD simulations, it would be beneficial to become familiar with the medical terminologies used to describe the anatomy of the nose and related structures.

2.1.1 Anatomical planes

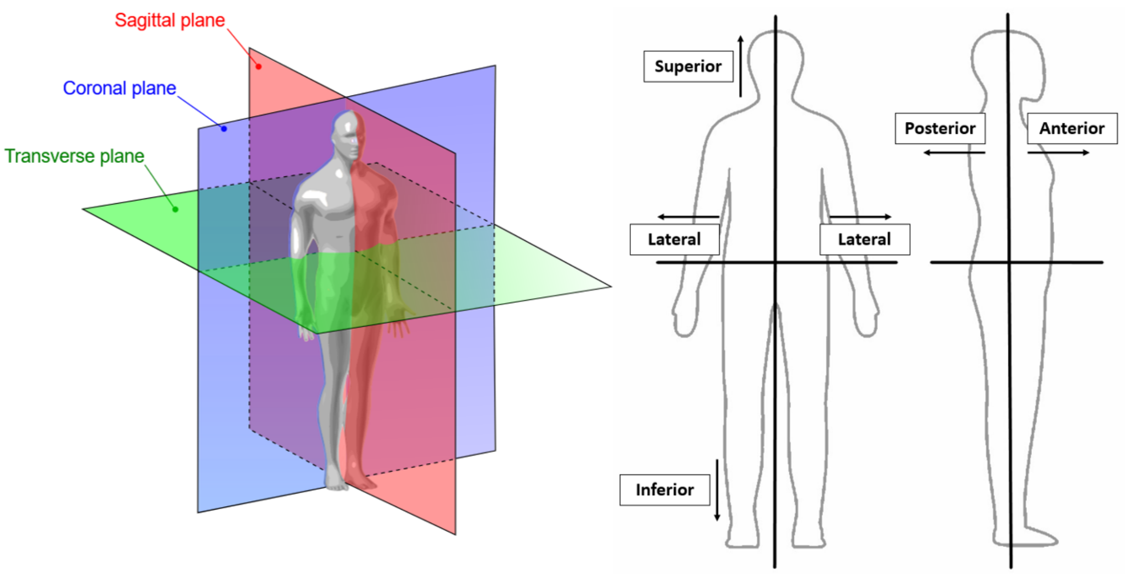

Figure 2.1: Anatomical planes and terminologies. Licensed under CC BY-NC-SA 3.0 US [17].

The accurate location of various organs or structures and the direction of movements inside the human body are described using the anatomical planes. These are the hypothetical planes that transect the body in an upright position. The reader must know these planes and several other terms used in the standard anatomical model.

The three principal planes used, as shown in figure 2.1, are listed below.

- Coronal plane - divides the body in anterior (front) and posterior (back) section

- Sagittal plane - divides the body in left and right (lateral) section
- Transverse plane - divides the body in superior (upper) and inferior (lower) section

2.1.2 Anatomy

Physiologically, the respiratory system of humans extends from the nostrils down to the lungs. It is the network of organs and tissues that helps us breathe. The respiratory system includes the airway, lungs, and blood vessels. For this project, we focus our attention on the upper respiratory tract as we aim to study the possibility of using CFD techniques to diagnose nasal obstructions. The upper respiratory tract consists of the nostrils, nasal cavity, paranasal sinuses, pharynx, and larynx.

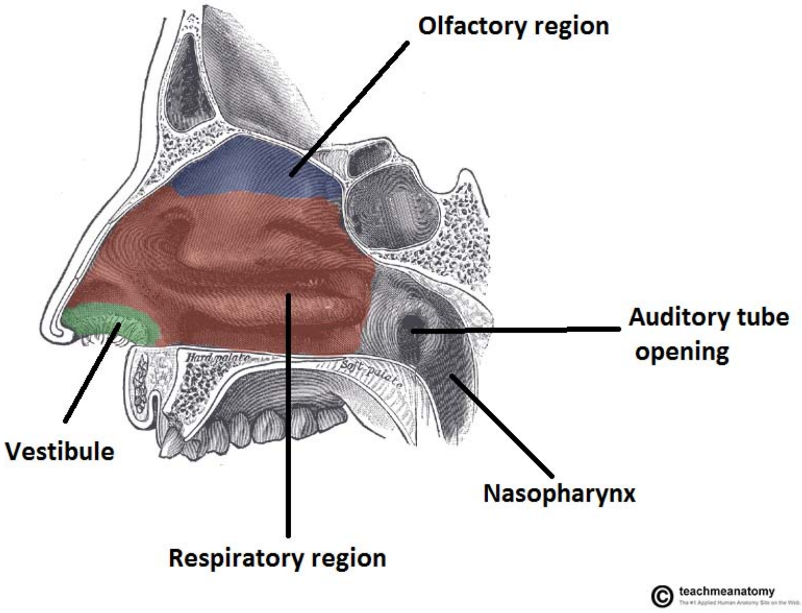

Figure 2.2: Divisions of the nasal cavity - sagittal view. Reproduced with permission by Oliver Jones [18].

The nasal cavities are elongated, wedge-shaped spaces with a large inferior base and a narrow superior apex located above the oral cavity and behind the nose. It communicates with the external environment via nostrils by providing a passageway for the inhaled/exhaled air to/from the rest of the respiratory system. As depicted in figure 2.2, the nasal cavity extends from the nasal vestibule to the nasopharynx and has three divisions:

- Nasal vestibule - Situated in the anterior portion of the nose where the air can enter into the respiratory system. The inhaled particles are filtered here because of the coarse hairs called vibrassae.
- Respiratory region - This region is covered in respiratory epithelium and mucous cells. The respiratory region functions to warm and humidify the inhaled

air along with filtering and eliminating the debris.

- Olfactory region - Situated at the apex of the nasal cavity. It is lined by olfactory cells with olfactory receptors.

The nasal septum located at the center of the node divides the cavity into two airways. Both these airways meet and form a single channel at the posterior end near the nasopharynx. The nasal cavity consists of several distinct parts - the roof, floor, medial wall, and lateral wall.

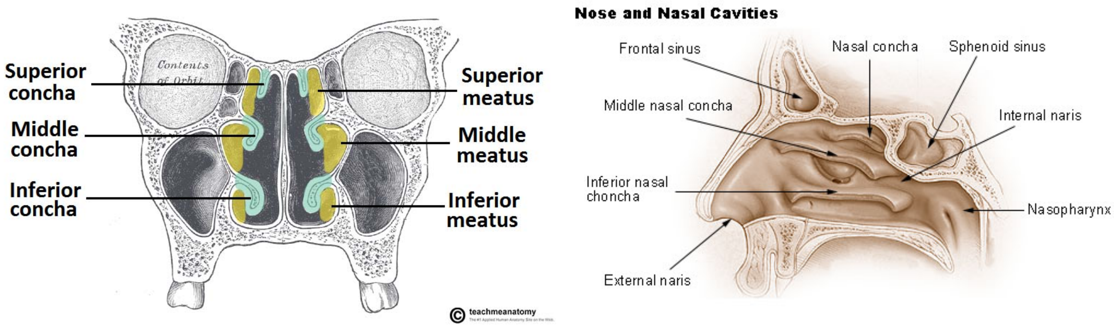

(a) Coronal view. Reproduced with permission by Oliver Jones [18].

(b) Sagittal view. Licensed under CC BY-SA 3.0 [19].

Figure 2.3: Turbinates and meatus in nasal cavity.

In the middle portion of the nasal cavity, curled bone structures project out from the lateral walls. They are called turbinates or conchae (singular - concha), and the three turbinates are classified as inferior, middle, and superior. The turbinates are covered with soft tissue and mucosa. Their primary function is to increase the surface area of the nasal cavity. As more inspired air comes in contact with the cavity walls, better will be the conditioning or humidification of the air. Due to the structure of the turbinates, the air path in the cavity curls as we go towards the posterior end of the cavity. The turbinates work to disrupt the laminar, fast-moving air to make it turbulent and slow, thus spending a long time in this region of the nasal cavity. The air path created by the turbinates are called meatus and are named corresponding to the location of the turbinates as,

- Inferior meatus - between inferior turbinate and floor of the cavity.

- Middle meatus - between inferior and middle turbinate.

- Superior meatus - between middle and superior turbinate.

The nasal cavity is surrounded by the paranasal sinuses - which are air-filled extensions of the nasal cavity. The four paranasal sinuses are frontal, ethmoid, maxillary, and sphenoid sinus. These sinuses are connected with the cavity on the roof or the lateral walls via ducts that drain through the Ostia. The geometry used for simulations in this project does not take into account these sinuses. It is because of the negligible flow in the sinuses compared to the mean flow in the nasal cavity during the breathing cycle.

A detailed discussion about the anatomy of upper respiratory tract can be found in articles by Sobiesk *et al.* [20] and Jones [21].

2.1.3 Functions

The nose is the first component of the upper respiratory tract that comes into contact with the surrounding air. It is an olfactory and respiratory organ responsible for carrying out a diverse range of functions, as listed below.

- Filtering of particles - Minute aerosolized particles from inspired air are trapped in the nasal mucosa which are cleared by the mucus secreted by columnar epithelium which lines the nasal cavity. [20]
- Conditioning of inspired air - The inhaled air needs to be warmed and humidified before it reaches the lungs. It is mainly done in the respiratory region, which is lined with ciliated pseudostratified epithelium. The air exchanges heat with the blood flowing in the blood vessels by convection, conduction, and radiation mechanism, thus raising its temperature. The moisture present in the mucus helps in the humidification of the air [22].
- Olfactory function - It occurs in the olfactory region which is lined with olfactory epithelium cells interspersed with neurons containing sensory cilia. Odorants trapped in the mucus binds with proteins which help to concentrate and solubilize the particles. These particles are then attached to the receptors on the cilia which transmit a signal to synapse with the neurons of the olfactory bulb, which eventually relays information to the brain via olfactory nerves [20, 22].
- To drain and clear the paranasal sinuses and lacrimal ducts.

2.2 Rhinomanometry

Rhinomanometry is an objective method to analyze the obstructions in the nasal cavity and is quantified by the doctors using Nasal Airway Resistance (NAR). A pressure-flow curve is an output from the rhinomanometer, see figure 2.4, which could be analyzed in several ways to obtain the value of nasal airway resistance.

There exist several different types of rhinomanometry - passive, where the air is forced through the nasal airway by an external force, and active, which relies on the patient's breathing. Additionally, the measurements could be taken either anteriorly or posteriorly. In posterior rhinomanometry, nasal resistance for the total cavity is obtained by positioning a probe in the nasopharynx via an air tube. Individual nasal resistance for each cavity (i.e., left and right) is obtained from anterior rhinomanometry. In this method, the probe is placed in the nasal vestibule, and the corresponding nostril is sealed using surgical tape. Thus, to complete measurement,

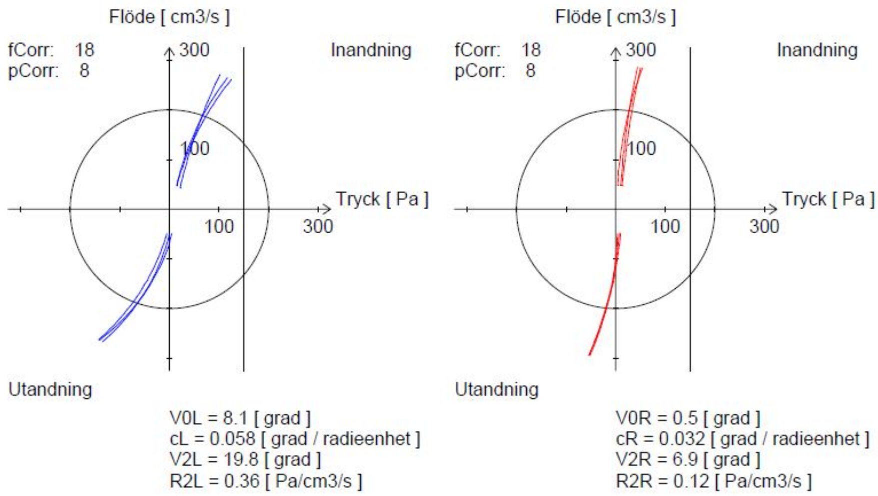

Figure 2.4: Pressure-flow curve as obtained from anterior rhinomanometry.

anterior rhinomanometry needs to be performed twice - once for each nostril. The nasal resistance for the total cavity is then calculated based on these values. In this study, active anterior rhinomanometry is performed to evaluate the NAR in the nasal cavity.

The two most common methods to evaluate NAR from the pressure-flow curve are the Classical and Broms method. The International Standardization Committee on Objective Assessment of Nasal Airway (ISOANA) recommended NAR to be calculated at a reference pressure of 75 or 150 Pa for Classical method [23, 24]. It also suggested that NAR calculated using Broms method is as good as Classical method [25].

The nasal airway resistance is calculated as $NAR = \Delta P/Q$, where ΔP is the pressure drop in the nasal cavity and Q is the volume flow rate. For the Classical method, the value of Q corresponding to a pressure drop of either 75 or 150 Pa - depending on the choice of reference pressure used to calculate the nasal resistance. Whereas, in Broms method, the pressure-flow curve is plotted on a polar coordinate system, and the value of ΔP and Q where the curve intersects a circle corresponding to $\Delta P = 200$ Pa is noted for computation of nasal resistance.

2.3 Computational Fluid Dynamics (CFD)

Computational Fluid Dynamics (CFD) is a branch of fluid mechanics in which a physical phenomenon involving fluid flow or heat transfer is modeled mathematically and solved using several computational methods. Using these methods, CFD provides a qualitative prediction of flow parameters based on conservation laws governing fluid motion [26].

2.3.1 Governing equations

The equations governing the mechanism of fluid flow are derived by applying the principles of conservation of mass, momentum, and energy on a control volume (or an infinitesimal fluid element) defined inside a fluid continuum.

2.3.1.1 Continuity equation

The governing equation resulting from the application of the mass conservation principle on the control volume or the fluid element is the *continuity equation.* The fundamental physical principle of mass conservation states that the mass must remain constant over time for a closed system, i.e.,

Rate of increase of mass in the fluid element	=	Net rate of flow of mass into the fluid element.

The conservative, differential form of continuity equation is given as

$$\frac{\partial \rho}{\partial t} + \frac{\partial(\rho v_i)}{\partial x_i} = 0, \tag{2.1}$$

where ρ is the fluid density, t is the time, v_i is the velocity in i-direction, and x_i denotes the spatial coordinate in i-direction [27].

If the flow is assumed to be incompressible, the density of the fluid remains constant. Then equation 2.1 is re-written as

$$\frac{\partial v_i}{\partial x_i} = 0.$$

2.3.1.2 Momentum equation

The application of the momentum conservation principle on the control volume or the fluid element gives the *Navier-Stokes equation* or *transport equation for momentum.* The momentum conservation principle is derived from Newton's second law, and it states that

Rate of increase of momentum of the fluid element	=	Sum of forces on the fluid element.

There are two major types of forces acting on the fluid particle - body forces (centrifugal, electromagnetic, and Coriolis force) and surface forces (pressure, viscous, and gravity force).

The momentum equation is given as [27]

$$\rho\frac{\partial v_i}{\partial t} + \rho\frac{\partial(v_i v_j)}{\partial x_j} = -\frac{\partial P}{\partial x_i} + \frac{\partial}{\partial x_j}\left[2\mu S_{ij} - \frac{2}{3}\mu\frac{\partial v_k}{\partial x_k}\delta_{ij}\right] + \rho f_i, \tag{2.2}$$

where P is the pressure, μ is the dynamic viscosity of the fluid, δ_{ij} is the kronecker delta, f_i is the body force in i-direction, and

$$S_{ij} = \frac{1}{2}\left(\frac{\partial v_i}{\partial x_j} + \frac{\partial v_j}{\partial x_i}\right).$$

Assuming an incompressible flow with constant density and constant dynamic viscosity of fluid, equation 2.2 is re-written as

$$\frac{\partial v_i}{\partial t} + \frac{\partial (v_i v_j)}{\partial x_j} = -\frac{1}{\rho}\frac{\partial P}{\partial x_i} + \nu \frac{\partial^2 v_i}{\partial x_j \partial x_j} + f_i,$$

where ν is the kinematic viscosity of the fluid.

3
Methods

In this chapter, the methodology followed for in-vitro experiments and CFD simulations are discussed. The reasonable choices made during these steps are justified, and the method to evaluate the nasal airway resistance is presented.

For this project, two different models of the nasal cavity were evaluated - the first (referred to as model 1) is modeled using anonymous CT-scans provided by Sahlgrenska hospital and the second (referred to as model 2) was available as a supplementary material in the research paper [16]. The CFD simulations and in-vitro rhinomanometry experiments are performed on both models of the nasal cavity. However, only model 2 was used for the in-vitro experiment to evaluate the pressure distribution in the nasal cavity.

3.1 Generate a 3D model from CT scan

The following tools were used to generate a 3D model from the CT scan data which has been further used to generate a computational mesh as well as a 3D model.

- 3D Slicer 4.11 - Open source software package
- Blender 2.91 - Open source software package
- Materialise Magics 25.01 - Commercial software package (a trial version available for student was used)

The nasal cavity model was reconstructed from CT scan slices available as Digital Imaging and Communications in Medicine (DICOM) files provided by Sahlgrenska hospital. An anatomically correct 3D model was derived in 3D slicer software by applying several segmentation techniques and strategies. The following steps were implemented in this software:

- Import the DICOM files in 3D Slicer.
- Switch to the ‘Volumes’ module and set the display to "CT-Air". It will emphasize the air in a CT volume.

- Switch to the 'Simple Filters' module and apply the Laplacian sharpening image filter. It enhances the image contrast and helps to distinguish the airway path and the soft tissues in the nasal cavity, see figure 3.1.

- Switch to the 'Segment Editor' module. Using the Threshold tool, set the thresholding interval to -1024 to -229 HU (Hounsfield Units). The software will highlight the CT volume within the given range of HU units and rebuild the highlighted section.

- To avoid the reconstruction of redundant areas like paranasal sinuses, any connection from this region to the nasal cavity airway had to be manually cut-off. The paint, scissors, and islands tools were utilized for this purpose.

- Generate the 3D model once the nasal cavity has been separated from other regions. Verify the anatomical correctness of the generated 3D model by visual inspection.

- Save the 3D model as an Standard Tessellation Language (STL) file, which is the desired format for mesh generation in OpenFOAM.

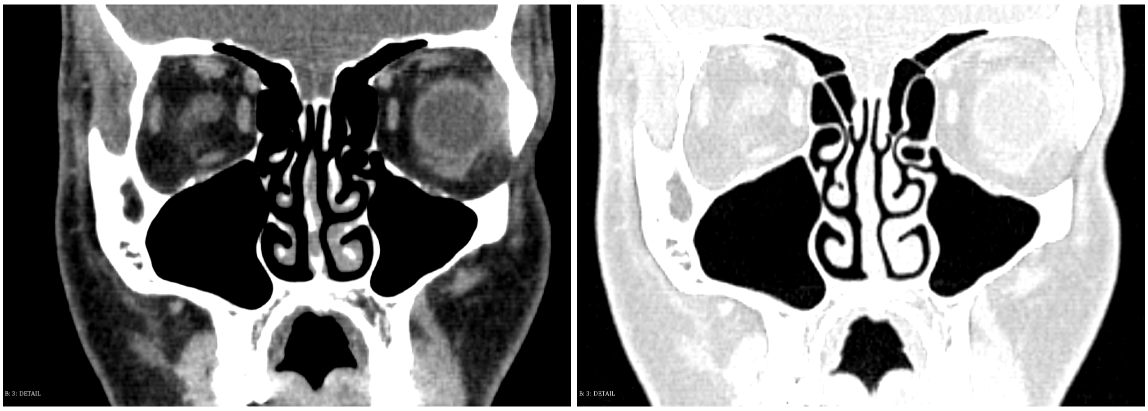

(a) Before applying the filter **(b)** After applying the filter

Figure 3.1: Coronal view of the CT scan.

The STL file from 3D Slicer was imported in Blender for further post-processing. The geometry was cleaned in Blender to prepare it for 3D printing as well as for generating a computational mesh. The holes or sharp edges in the model were filled and smoothed. Additionally, to ensure the anonymity of the patient, changes were made to the original face obtained from the CT scan using the sculpting tool in Blender. Changes near the nose and upper lip were avoided since it could alter the path of the incoming air in the nasal cavity.

Further, the 3D printing toolbox in Blender and Materialise Magics were used to fix the errors related to the 3D printing of the model. Once the model was completely checked and free of any errors, a 1 mm wall thickness was added to the model for 3D printing. The nasal cavity was printed in ClearVue using the Stereolithography (SLA) method. The 3D printed nasal cavities are shown in figure 3.3.

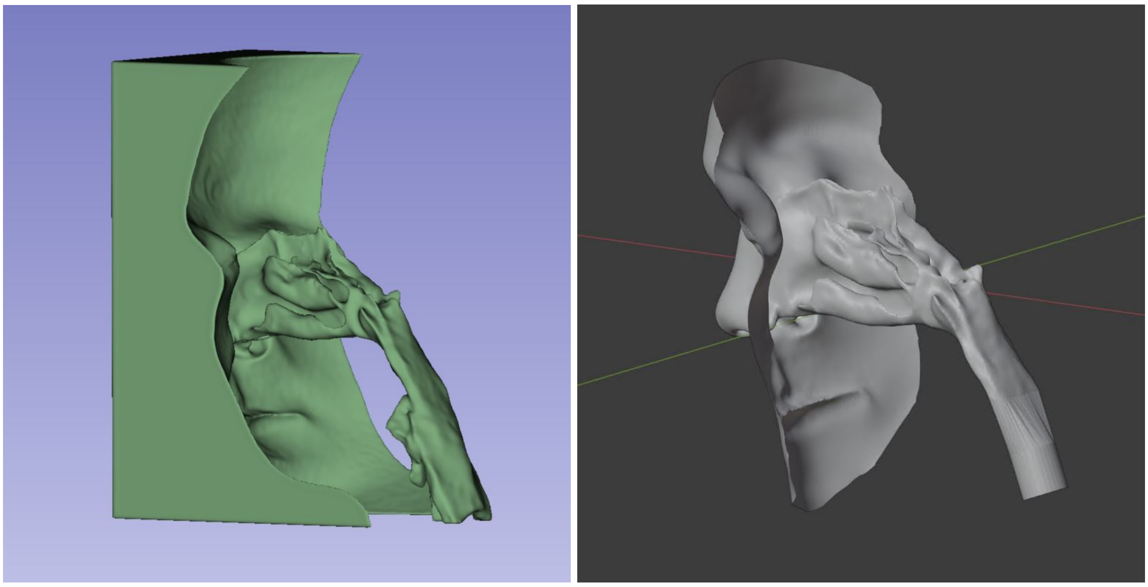

(a) after segmentation in 3D Slicer (b) after geometry cleaning in Blender

Figure 3.2: 3D model of nasal cavity.

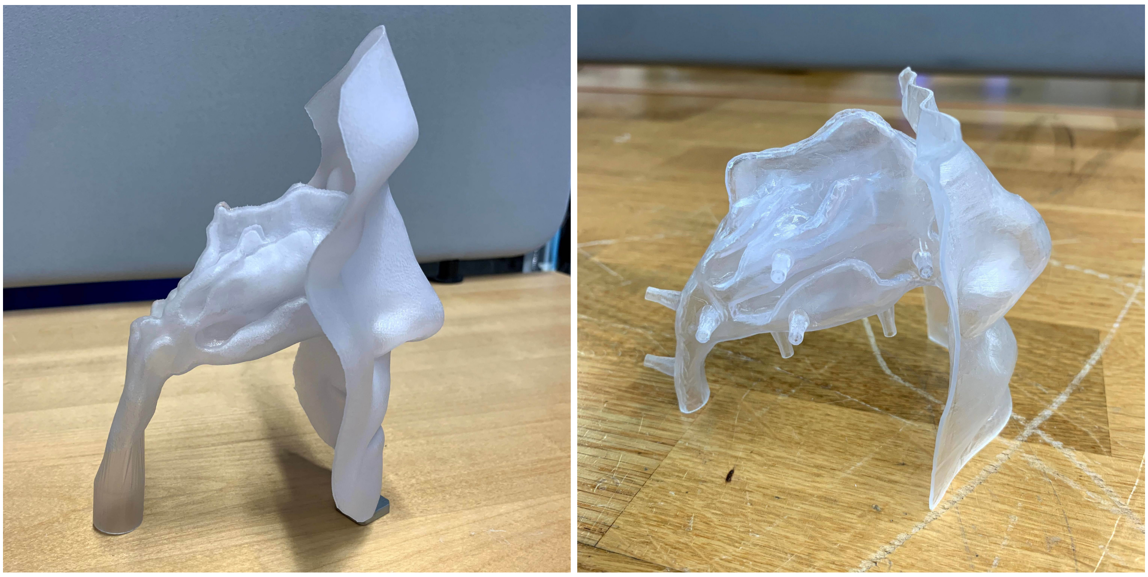

(a) Model 1 (b) Model 2

Figure 3.3: 3D printed nasal cavity.

3.2 Experiments

To gauge the validity of the numerical model, it is important to compare the results with experimentally obtained data. Hence, in-vitro experiments are carried out in this project to compare and determine the accuracy of the simulation results.

The flow rate during tidal breathing at rest in humans can be exhibited by the curve as shown in figure 3.4, and it varies with the physiological condition of an individual.

Using suitable boundary conditions in CFD simulations, one can yield a similar flow rate corresponding to the actual breathing cycle of humans. However, to generate the same for experiments is difficult. Hence, an assumption is made that the tidal breathing is fairly sinusoidal, and a simplified flow rate curve is used for experiments and simulations.

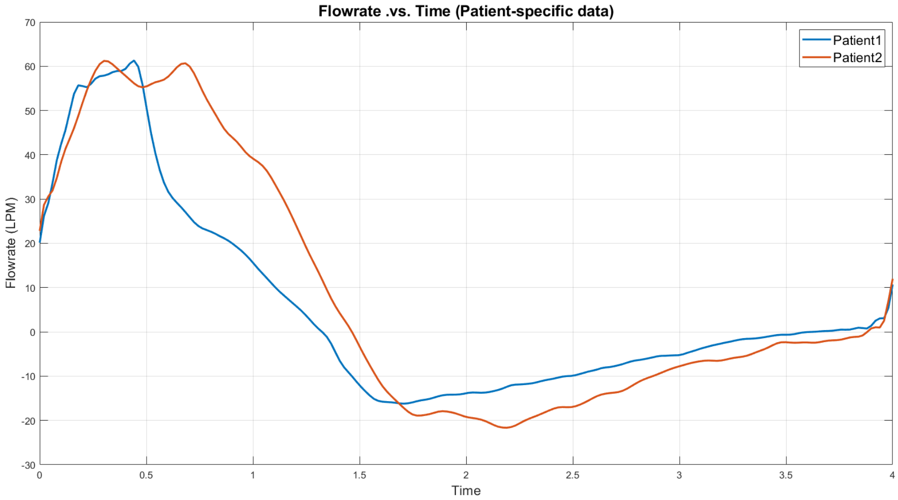

Figure 3.4: Tidal breathing flow rate curve observed in humans - averaged over several breaths. Data corresponds to anonymous patients provided by Sahlgrenska hospital.

To recreate the tidal breathing cycle (inhalation and exhalation) during the experiments, it is necessary to build an experimental rig that would act as an artificial lung. The concept of a simple slider-crank linkage was applied to facilitate such a mechanism of tidal breathing. Figure 3.5 shows the schematic representation of the experimental setup.

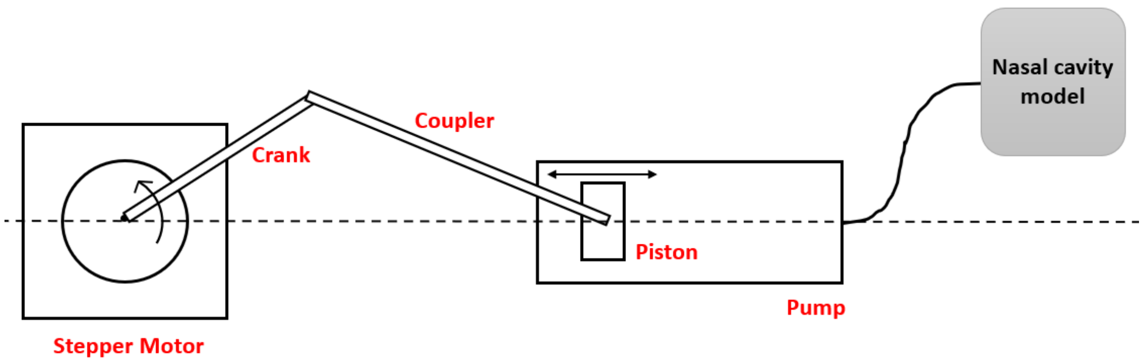

Figure 3.5: Schematic representation of the experimental rig.

A stepper motor operated using a "Geckodrive G230V" motor driver receives an electrical pulse signal from an oscillator. The frequency of the pulse is set to 500 Hz to have the motor speed as 0.25 revolutions per second, which is equivalent to a tidal breathing duration of 4 seconds. The motor shaft is connected to a crank, and further, it links the coupler of the slider-crank mechanism to a piston situated inside a pump. The piston will reciprocate to produce an inhalation-exhalation cycle in the nasal cavity attached to the pump via a silicone hose. The velocity of the piston will follow a curve defined by

$$v = -r.sin(\theta) + \frac{r^2.sin(\theta).cos(\theta)}{\sqrt{l^2 - r^2.sin^2(\theta)}},$$

where, v is the piston velocity, r is the crank length, and l is the coupler length. Due to the assumption that air is incompressible, the flow rate from the pump will also follow a similar curve. Thus, the shape of the curve can be changed by varying either the crank or coupler length or both. In this experimental setup, the crank length is kept variable. Therefore, the artificial lung can be operated to provide several breathing cycles with a mean flow rate varying from 10-30 Liters per Minute (LPM). Several breathing profiles were used for simulations and experiments to check the variability of the nasal resistance when a different breathing profile is used. It resembles the actual conditions since it is difficult for humans to reproduce the same breathing profile for consecutive rhinomanometry measurements. Figure 3.6 shows various flow rate curves used for in-vitro rhinomanometry and pressure measurement experiments.

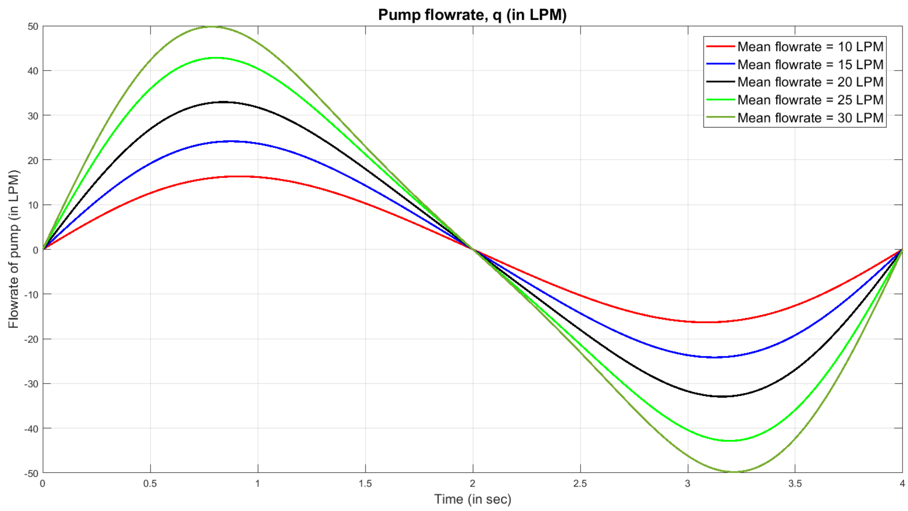

Figure 3.6: Tidal breathing flow rate curve - obtained by varying crank length in the experimental rig.

3.2.1 In-vitro rhinomanometry

The nasal airway resistance was measured in-vitro for both the nasal cavity models using a rhinomanometer (Rhino-Comp/®M, IBBAB, Billdal, Sweden) acquired from Sahlgrenska hospital, see figure 3.7. The face mask is used to form a tight seal between the face and the surroundings to avoid leakages. Considering that the surface of the 3D printed cavity is hard as opposed to actual human skin, leakages occurred due to non-conformity between the 3D printed nasal cavity and the face mask. Hence, modeling clay was used to form an intermediate surface to form a tight seal and avoid leakages.

Figure 3.7: Rhinomanometer.

Since an active anterior rhinomanometry was performed, one nostril was blocked using surgical tape. The device then measures the pressure inside the blocked cavity using a probe that passes through the surgical tape and rests inside the nasal vestibule. The data over three tidal breaths is recorded and averaged out to produce a pressure-flow curve similar to the one in figure 2.4. The same steps are repeated by blocking the other nostril. Combining these two measurements, the nasal airway resistance is obtained for the total nose.

The values from the pressure-flow curve correspond to the pressure drop between the cavity and surroundings. The readings are taken based on the following assumption - the pressure inside the blocked cavity does not vary due to the absence of flow, and hence the pressure at the nasopharynx can be assumed to be equal to the pressure measured by the probe at the nasal vestibule.

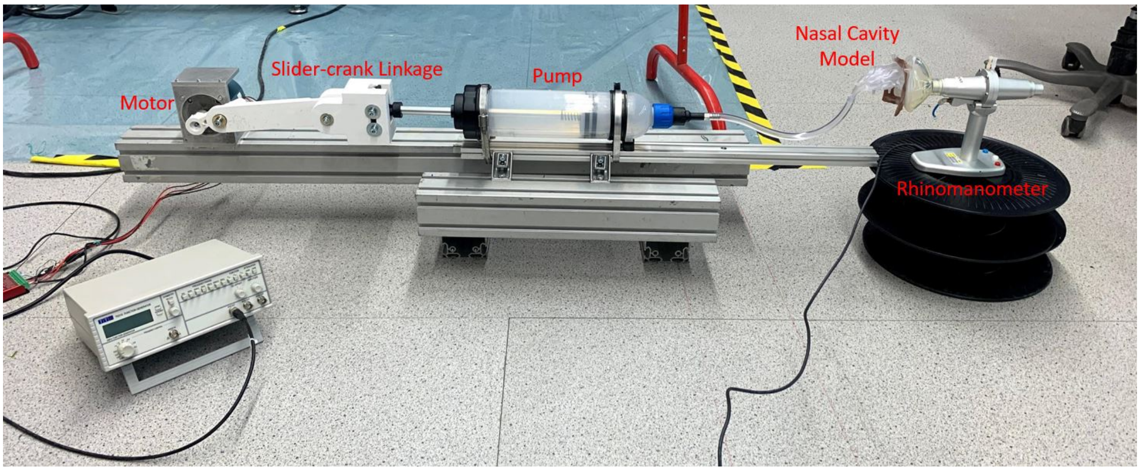

Figure 3.8: Experimental setup for rhinomanometry measurements.

3.2.2 In-vitro pressure measurements

This experiment was performed only for model 2. The pressure distribution inside the nasal cavity was measured at locations where the externally extruding ports are located as seen in figure 3.3a.

The ports are located symmetrically in right and left cavities. There are a total of 14 ports - three along the nasal cavity floor on each side, four on the lateral walls of both sides, and two ports in the posterior of the cavity, see figure 3.9 for labeling of the pressure ports.

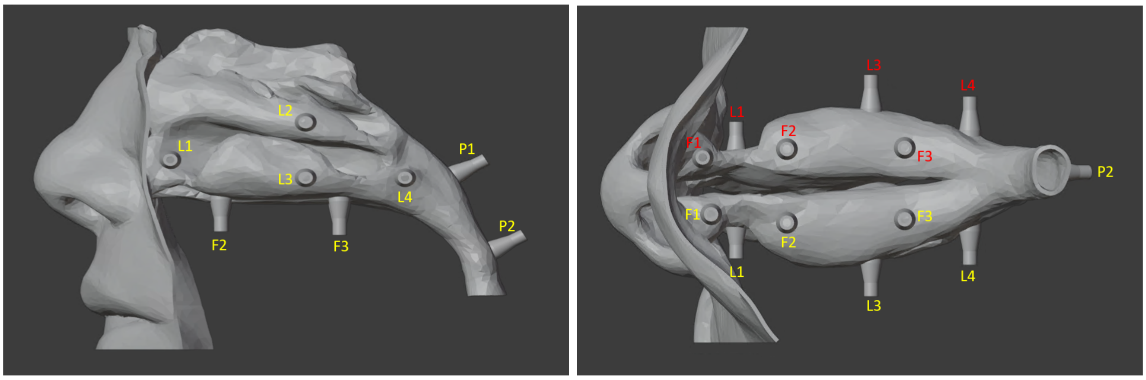

Figure 3.9: Location and labeling of pressure probes on the nasal cavity.

A 16-channel digital pressure scanner (PSI-9116, Pressure Systems, Inc.) with a 500-Hz sampling rate was used to acquire pressure values. Pressure transducers were connected by hoses at the probe locations to gather data. A sampling window of 100 seconds was kept and the pressure drops at these locations were sampled at a rate of 500 Hz. Finally, ensemble averaging was performed over the data to obtain the pressure drop over a single tidal breath. The experimental setup is shown in figure 3.10.

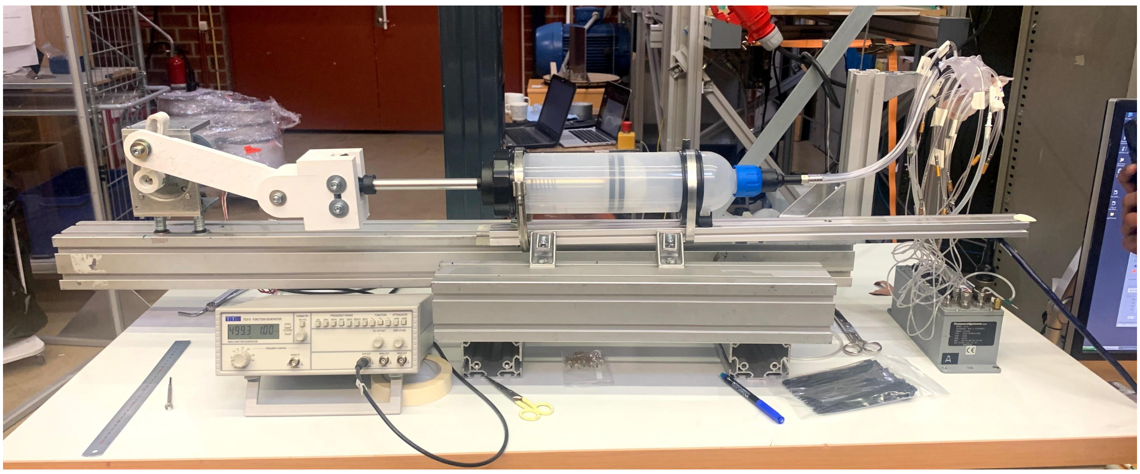

Figure 3.10: Experimental setup for pressure measurements.

3.3 CFD simulation

The open-source software OpenFOAM® v2006 was used for the CFD simulations. In this section, the methodology to perform the simulations is discussed.

3.3.1 Geometric model

To prepare the nasal cavity model for CFD simulations, the surface STL file as shown in figure 3.2b is further modified to make it water-tight. The nasopharynx is elongated at the exit to facilitate the fit of the pipe to connect the 'artificial lung' for experiments.

The face and the external nose are generally excluded for the CFD simulations, and the air inflow is directly specified at the nostrils [13, 28, 29]. That reduces the mesh count in the domain. However, Taylor *et al.* [30] found that the inflow geometry truncation affects the downstream flow in the nasal cavity. It is essential to include the external facial features, as it would allow the natural inspiration of air into the nasal cavity. Hence, to recreate the normal breathing scenario from the surroundings, a hemisphere is constructed in front of the face. The external facial features are included in the computational domain, but it will increase the number of meshing elements. The final geometries used for CFD simulations are shown in figure 3.11.

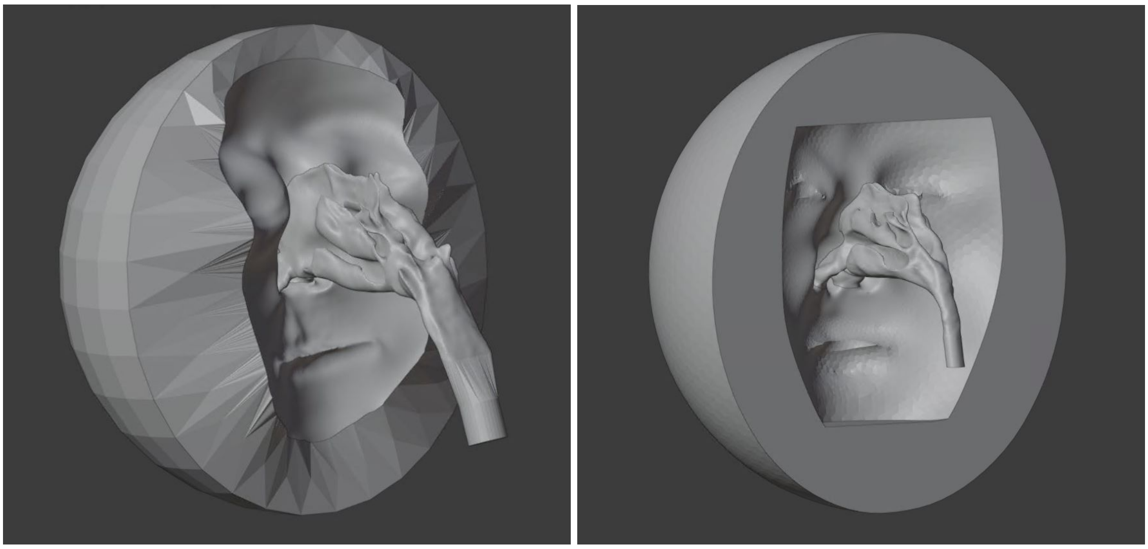

(a) Model 1 - from CT scan **(b)** Model 2 - from Strien *et al.*

Figure 3.11: Geometric model for CFD simulation.

3.3.2 Flow physics and solver settings

A transient simulation with time-varying flow rates is performed to mimic the tidal breathing condition in humans. The flow is assumed to be incompressible due to the velocities being very low. In OpenFOAM® v2006, particular dictionaries are mandatory to completely define the physics of the problem and the methods required to solve them.

- `controlDict` is used to specify the case controls for the simulation. This dictionary includes time-stepping information, write format, and additional user-defined functions for post-processing.

- The properties of the fluid are specified in `transportProperties` dictionary, while the choice of turbulence model is given in `turbulenceProperties` dictionary.

- The numerical schemes used to solve various terms of the discretized governing equation are specified in `fvSchemes` dictionary.

- `fvSolution` dictionary contains the instructions on how each discretized equation is solved. The equation solvers, tolerances, and algorithms are controlled from this file.

The average breathing rate in humans is 10-15 breaths per minute. Hence, the duration of a tidal breath is assumed to be 4 seconds in this project. Two consecutive tidal breaths were simulated, i.e., a total simulation time of 8 seconds. The results from the second cycle are considered for post-processing to account for the inertial effects (hysteresis) associated with the time-varying boundary conditions [12, 31]. A time-step of 10^{-5} seconds was defined at the start of the inhalation and exhalation period. After 200 iterations, the time-step was gradually increased to 10^{-3} seconds. A sudden change in the direction of the velocity vectors at the outlet boundary can cause the solution to diverge. Hence, smaller time-steps were used at the start of the inhalation and exhalation period. A maximum time-step of 10^{-3} seconds was adapted during the simulation.

The working fluid in consideration is air with a density (ρ) of 1.225 kg/m^3 and a dynamic viscosity (μ) of 1.79×10^{-5} $Pa.sec$. For the transient tidal breathing simulations, no turbulence model is used and this choice is explained in section 3.3.2.1.

The time-derivative term in the governing equation is discretized using the implicit second-order `backward` scheme. The convective terms were resolved using the `linearUpwind` scheme, which is second-order bounded in nature. The gradients were calculated using the second-order `leastSquares` method. A linear interpolation scheme was employed to interpolate values from cell centers to face centers. The `fvSchemes` dictionary is specified in Appendix A.3.

The pressure-velocity coupling is achieved using the PIMPLE (Pressure Implicit with Splitting of Operators) algorithm. The pressure equation is solved using `GAMG` solver while the equations for velocity use `smoothSolver`. The `fvSolution` dictionary can be seen in Appendix A.4.

3.3.2.1 Justification for not using a turbulence model

Tidal breathing is unsteady and transient, where the flow rate accelerates from zero to a peak value followed by deceleration back to zero. Thus, the flow fluctuations in the nasal cavity are induced from the complex geometry features as well as the temporal unsteadiness due to the continuous accelerating-decelerating nature of tidal breathing flow [32]. These fluctuations must be captured in the CFD simulations. Lee *et al.* [12] and Calmet *et al.* [14, 32] simulated the respiratory flow in the nasal passage using the LES method and were able to provide the solution of the flow field with a considerable accuracy due to a better capability of the LES method in treating the transient terms of the governing equations. However, LES simulations are computationally expensive, and they are not suitable for studies involving several simulations due to time constraints.

Calmet *et al.* [32] used the LES simulation as a reference case for comparison with lower resolution models that included larger time-steps, as well as no turbulence modeling, [32]. The pressure drop values were similar for the simulation without turbulence model when compared with the LES simulation. Additionally, a comparison of instantaneous and mean flow velocity contours between both models showed very similar patterns. The authors concluded that the lower resolution models with no turbulence modeling provide sufficient accuracy when interested in overall trends like pressure drop and mean velocity fields. Based on the results from this study, it was decided not to use any turbulence model for the simulations in this project. Instead of modeling the small-scale turbulent structures, they were allowed to be resolved based on the mesh resolution and the time-step.

3.3.3 Computational mesh

The next step in CFD methodology after pre-processing the CAD model is to generate a computational mesh. Meshing is the process in which a complex CAD model is divided into several smaller elements. The governing equations are solved in each of these discretized elements to determine the flow variables in the entire domain. A detailed mesh will help to have a better representation of the CAD model. However, it would increase the number of elements. It would lead to a significant increase in computational time for the simulation. Hence, it is necessary to find an appropriate mesh that can provide an acceptable solution without excessive usage of computational resources. The computational mesh was generated in the open-source software OpenFOAM® v2006 using the *blockMesh* and *snappyHexMesh* utilities.

3.3.4 Boundary conditions

The three boundaries for the CFD geometry - atmosphere, wall, and throat are depicted in figure 3.12. During inhalation, the atmosphere boundary acts as an inlet and the throat boundary is the outlet. These boundaries behave the other way round during the exhalation period. A total pressure boundary condition is specified at the atmosphere boundary. At the posterior section, the nasal cavity model is truncated at the nasopharynx. This section is extended further to avoid re-circulation during simulations and also for experimental purposes. The unsteady tidal breathing flow rate is specified at the throat boundary using the flowrate boundary condition. The nasal cavity and the face are modeled as a no-slip wall. The summary of boundary conditions specified in `p` and `U` dictionaries for OpenFOAM is given in table 3.1. The complete `U` and `p` dictionaries are given in Appendix A.1 and Appendix A.2 respectively.

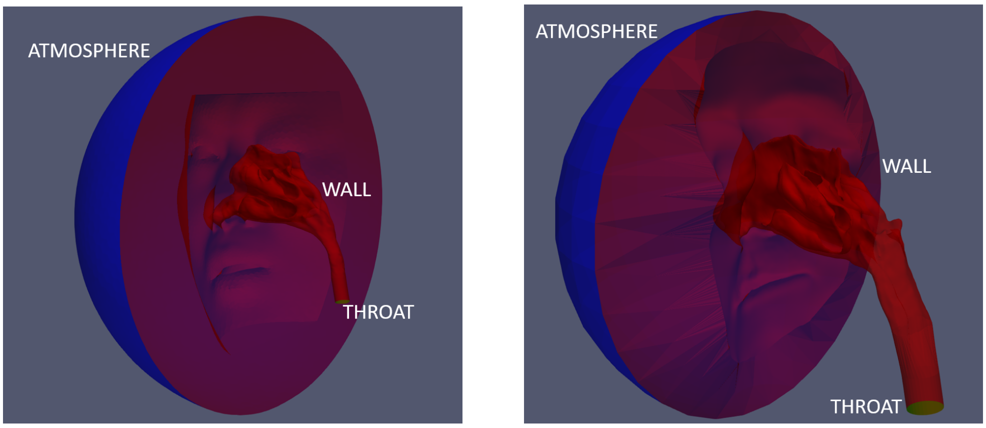

(a) Model 1 **(b)** Model 2

Figure 3.12: Boundaries for the CFD model.

Table 3.1: Boundary conditions for CFD simulations.

Boundary	**Type**	**Boundary condition**	
		p	**U**
Atmosphere	Total pressure	`totalPressure`	`pressureInletOutletVelocity`
Throat	Flowrate	`zeroGradient`	`flowRateOutletVelocity`
Wall	Wall	`zeroGradient`	`noSlip`

The tidal volume is the amount of air that moves in and out of the lungs during each respiratory cycle. The average tidal volume for an adult is 500 mL [33]. Figure 3.13 indicates the tidal breathing flow curves used for the simulations. The flow curve corresponding to a mean flow rate of 15 LPM has a tidal volume of 500 mL, and this flow curve is used for simulation of both the nasal cavity models. The flow curve with a mean flow rate of 25 LPM has a higher tidal volume and is used only for the simulation of nasal cavity model 1.

3.4 Mesh convergence study

3.4.1 Mesh study - model 1

A mesh convergence study was performed to determine a suitable mesh for this particular nasal cavity model. This study aimed to determine a computational mesh that would yield a negligible change in the solution with further refinement. An initial mesh was created such that all the fine details and the surfaces of the nasal cavity are represented by the mesh without any holes or discontinuities. The base

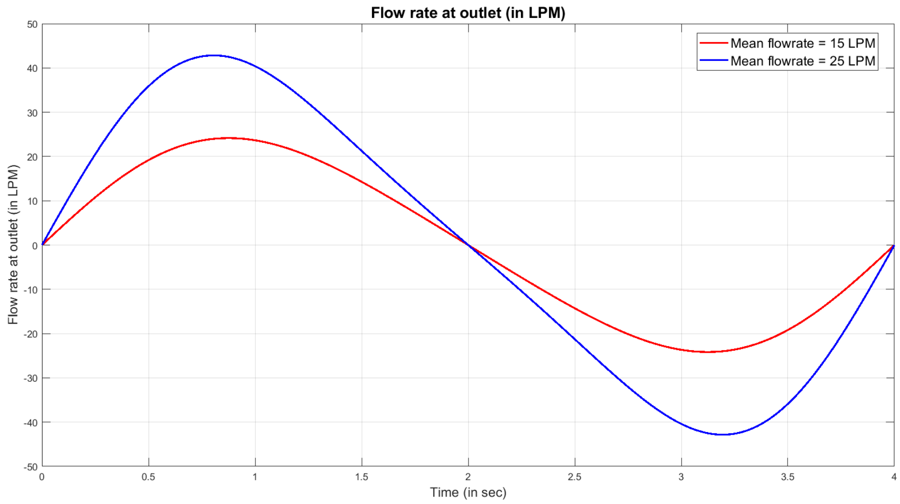

Figure 3.13: Tidal breathing curves specified at outlet.

mesh is further refined to create two more meshes for the study. The parameters used for generating the three meshes are summarized in table 3.2.

Table 3.2: Meshing parameters for mesh study - model 1.

	Mesh 1	**Mesh 2**	**Mesh 3**
Grid size - Δ_{min}	0.25 mm	0.20 mm	0.175 mm
Number of prism layers		5	
Height of 1^{st} prism layer		0.02 mm	
Total number of mesh elements	13.12 million	19.84 million	28.71 million

A suitable local or global flow parameter can be selected to perform the study. If the value of the flow parameter does not change significantly with the refinement of mesh, then the solution is said to be mesh-independent. A global flow parameter such as pressure drop across the nasal cavity is not suitable to judge the convergence as it can miss the regions of local poor mesh. Tracking the flow parameters on multiple probe locations or a single line ignores the rest of the domain. Hence, the mean velocity was monitored on multiple line profiles across multiple cross-section planes. This method ensures sufficient mesh independence as proposed by Inthavong et al. [34] in their research paper.

A steady-state simulation was performed with a constant flow rate of 30 LPM. The simulation was allowed to run for 5000 iterations, and the flow parameters were averaged over the last 2000 iterations to discard the initial transients. The mean velocity averaged over the 2000 iterations for all three meshes is plotted at several lines on multiple planes. The results from the mesh convergence study are discussed in section 4.1.1.

3.4.2 Mesh study - model 2

A mesh convergence study was performed by Strien *et al.* for this model of the nasal cavity in their research paper. Hence, it was decided to use the same parameters as given in the literature to generate the computational mesh. Since the meshing software was different, the overall meshing strategy and the number of elements were not similar to that obtained in [16]. The results from this mesh were compared with the literature to determine the validity of the mesh. The meshing parameters used for this nasal cavity model are tabulated in table 3.3. A total of 16.4 million mesh elements were generated using these parameters.

Table 3.3: Meshing parameters for mesh study - model 2.

Meshing software	blockMesh and snappyHexMesh
Grid size - Δx_{min}	0.125 mm
Grid size - Δy_{min}	0.165 mm
Grid size - Δz_{min}	0.185 mm
Number of prism layers	8
Height of 1^{st} prism layer	0.02 mm
Number of elements	16.4 million

A transient simulation for a duration of 0.35 seconds was performed on this mesh. A constant flow rate of 10, 15, and 30 LPM was used as a boundary condition at the outlet. It is similar to the simulations done by [16]. For simulating these cases, no turbulence modeling was done. The results were obtained by averaging the flow variables from 0.2-0.35 seconds. The results from this study are discussed in section 4.1.2.

3.5 Steady state solution .vs. tidal breathing simulation

Tidal breathing is a cyclic, oscillatory phenomenon. To accurately capture the flow features inside a nasal cavity, transient simulation with a time-varying flow rate boundary condition is needed. However, such simulations are required to run for a minimum of two breathing cycles [12, 31], and therefore the simulations become computationally expensive and time-consuming. Sometimes, the clinicians do not require a detailed analysis of the flow inside the nasal passage and are more interested in the overall trends like pressure drops and mean flow field. In such situations, simulations with rapid computations are preferred for investigating the flow through the nasal cavity. Therefore, steady-state simulations are performed, which are quicker compared to transient tidal breathing simulations. But first and foremost, it is essential to evaluate whether modeling the nasal cavity flow using the steady-state assumption is sufficient to describe the airflow and physiological performance of the nasal cavity.

The presence of inertial effect inside the nasal passage arising due to dynamic variation of flow with time indicates that the steady-state assumption is inappropriate. However, several studies [35, 36] have used steady-state solutions to analyze the nasal cavity flow. By studying the Womersley number and Strouhal number, they assumed the cyclic, unsteady flow in the nasal cavity to be quasi-steady. Womersley number (Wo) correlates the transient inertial forces with viscous forces, and the Strouhal number (St) is the ratio of inertial forces due to local acceleration of flow to the inertial forces due to convective acceleration [37]. These non-dimensional numbers are defined as

$$Wo = \frac{D}{2}\left(\frac{\omega}{\nu}\right)^{0.5} \quad \text{and} \quad St = \frac{\omega L}{u_{ave}},$$

where, D is the characteristic length which is taken as the hydraulic diameter of a cross-section near the nostril, ω is the breathing frequency equal to $\omega = 2\pi f = 1.57$ s^{-1} (f corresponds to 15 breaths per minute), ν is the kinematic viscosity of the fluid, L is the airway length in axial direction, and u_{ave} is the average velocity through the nasal passage.

The Womersley number (Wo) and Strouhal number (St) computed for model 2 of the nasal cavity were 1.7 and 0.05 respectively. The study by Isabey and Chang suggests that the quasi-steady assumption is valid for $St < 1$ and $Wo < 4$ [38]. Several values of non-dimensional numbers are used as a threshold, Doorly *et al.* [35] used $Wo = 3$ and $St = 0.25$, Shi *et al.* [37] used $Wo = 4.3$ and $St = 0.2$, while Wen *et al.* [36] used $Wo = 1.68$ and $St = 0.01$ as a criteria to define the quasi-steady state for nasal airflow. Thus, based on the Womersley and Strouhal number obtained in this study, it is reasonable to disregard the hysteresis effect and the flow could be modeled using a steady-state assumption.

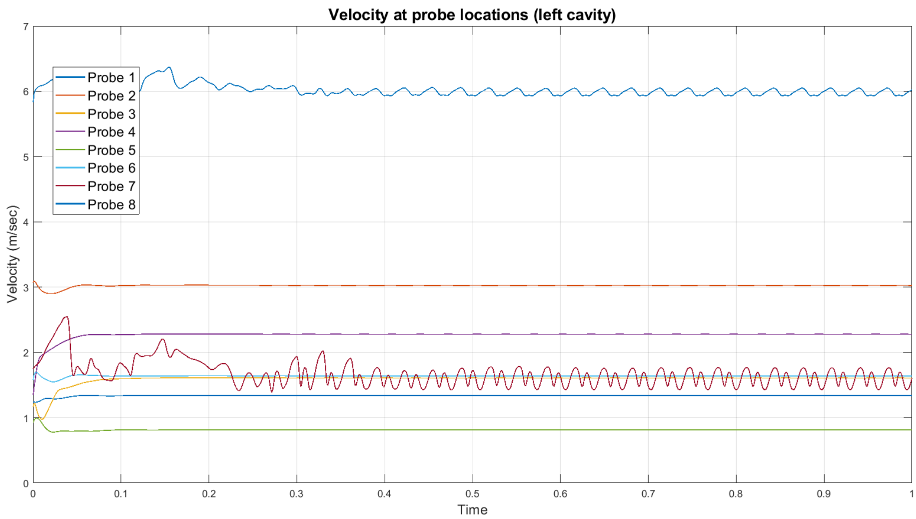

Figure 3.14: Velocity at probe locations in left cavity - transient constant flow rate simulation.

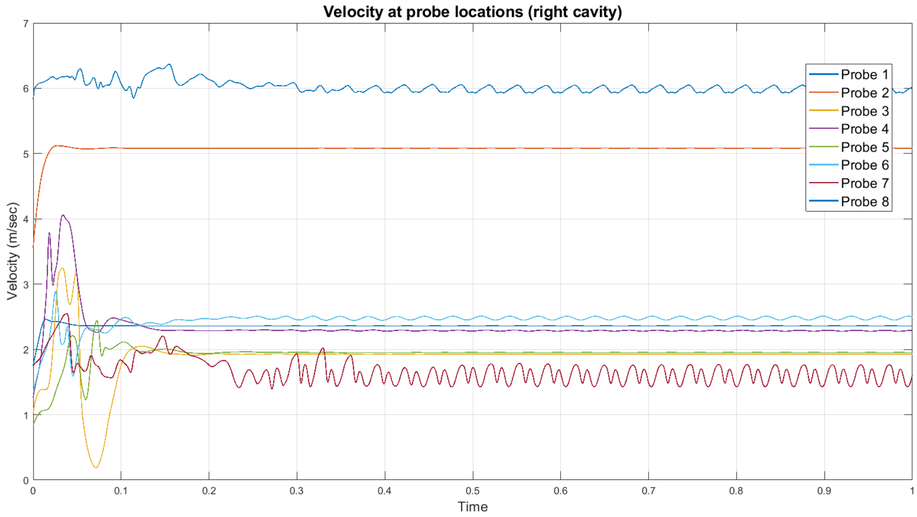

Figure 3.15: Velocity at probe locations in right cavity - transient constant flow rate simulation.

Initially, a steady-state simulation was performed, but a divergence in solution was observed for the simulations corresponding to the exhalation phase. Hence, it was decided to carry out a transient simulation with a constant flow rate boundary condition. The transient simulation was allowed to run long enough to achieve a steady-state solution. Probes were defined inside the nasal cavity at several locations to check the convergence of the simulation to a steady state. The velocity at these locations was monitored over time, and the results for one such simulation are seen in figures 3.14 and 3.15. Thus, it was concluded that the transient simulation converges to a steady-state solution in 1 second. The mean flow velocity and mean pressure were calculated by averaging the data from 0.5-1 second. The results from this comparison are discussed in section 4.5.

3.6 Evaluating nasal airway resistance

The nasal airway resistance in this project was calculated based on the Broms method as explained in section 2.2.

3.6.1 CFD derived nasal resistance

Nasal airway resistance can be calculated using the simulation results analogous to the values obtained by rhinomanometry. CFD simulations were performed for three cases - both nostrils open, right nostril blocked, and left nostril blocked. It is similar to rhinomanometry, where each nostril is blocked simultaneously. The flow rate and the corresponding pressure drop values in the nasal cavity were obtained from the simulations. These values were used to plot a fitted pressure-flow curve in cartesian and polar coordinates for each case. Figure 3.16 shows an example of fitted flow-curve obtained from CFD results. The nasal airway resistance is calculated using either of the methods suggested by Broms *et al* [25].

- From pressure-flow curve in cartesian cordinates - $NAR = \Delta P/Q$, where ΔP and Q are the values corresponding to the intersection point of the fitted curve and a circle with radius 200 Pa.
- From pressure-flow curve in polar cordinates - $NAR = 1/tan[(\theta_{in} + \theta_{ex})/2]$, where θ_{in} and θ_{ex} are the angles made by the pressure-flow curve at radius of 200 Pa in polar coordinates during inhalation and exhalation respectively. The angles were calculated by making use of the equation defining the fitted rhinomanometry curve.

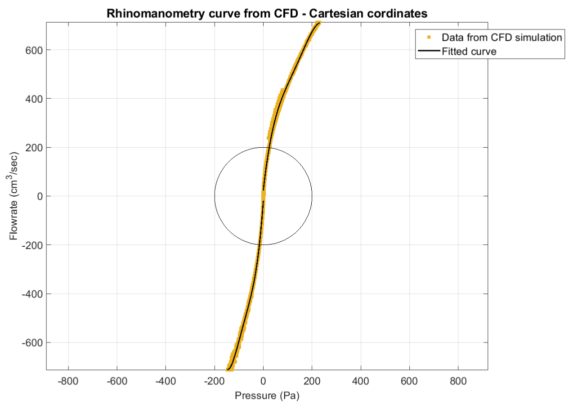

(a) In cartesian coordinates

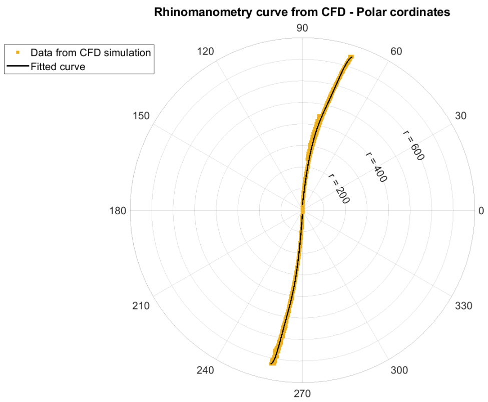

(b) In polar coordinates

Figure 3.16: Rhinomanometry curves reproduced from CFD results.

3.6.2 In-vitro rhinomanometry nasal resistance

To obtain the in-vitro rhinomanometry nasal resistance values, the experiment was performed to note 20 consecutive readings. The final nasal resistance was obtained by averaging these values. The rhinomanometer provides the nasal resistance value for an individual - left and right, as well as the total nasal cavity.

4

Results

In this chapter, experimental results are compared with the data obtained from CFD simulations. The pressure distribution inside the nasal cavity is analyzed to validate the CFD model. The in-vitro and in-silico nasal airway resistance is compared as well. The flow patterns observed during tidal breathing are also discussed in detail.

4.1 Mesh convergence study

4.1.1 Model 1

The location of the lines and planes along with the mean velocity plots are shown in figures 4.1-4.4.

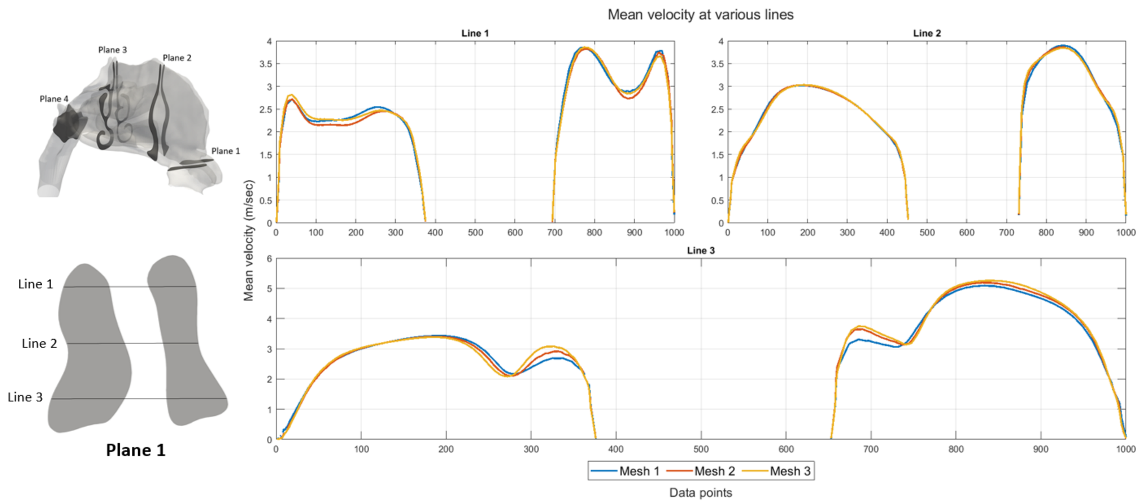

Figure 4.1: Line plots of mean velocity - plane 1.

Figure 4.1 shows the plane in the anterior part of the nasal cavity near the nasal vestibule. The mean velocity for all three meshes appear to be similar. On line 3, the mean velocity for mesh 2 and 3 near the septum wall seems close to each other.

Figure 4.2 shows the location of plane 2 in the nasal cavity. The mean velocities are similar on lines 1 and 2 for all meshes (flow in the vicinity of line 1 can be assumed to be negligible). On line 3, the values on mesh 2 and 3 are alike. However, in the

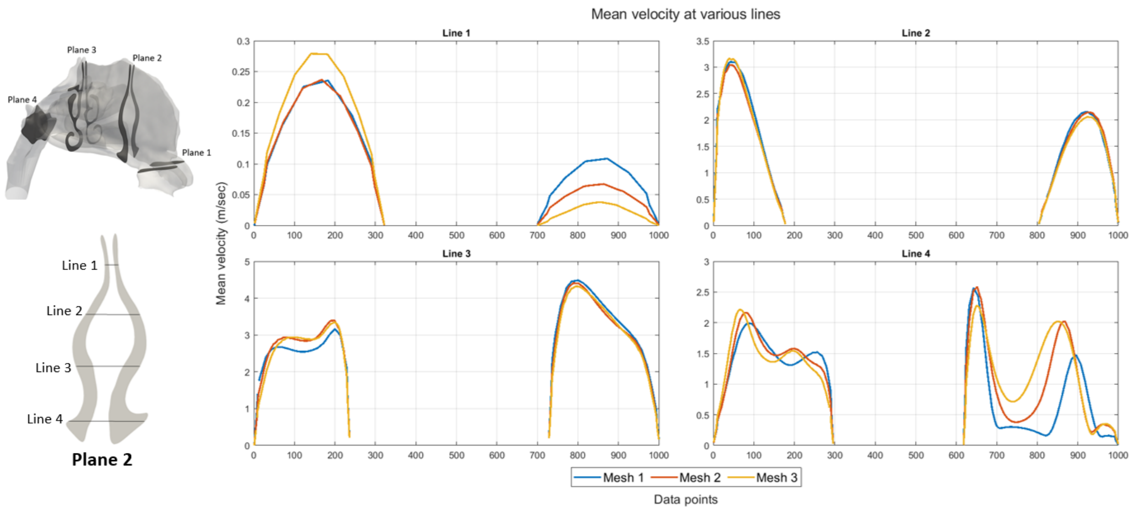

Figure 4.2: Line plots of mean velocity - plane 2.

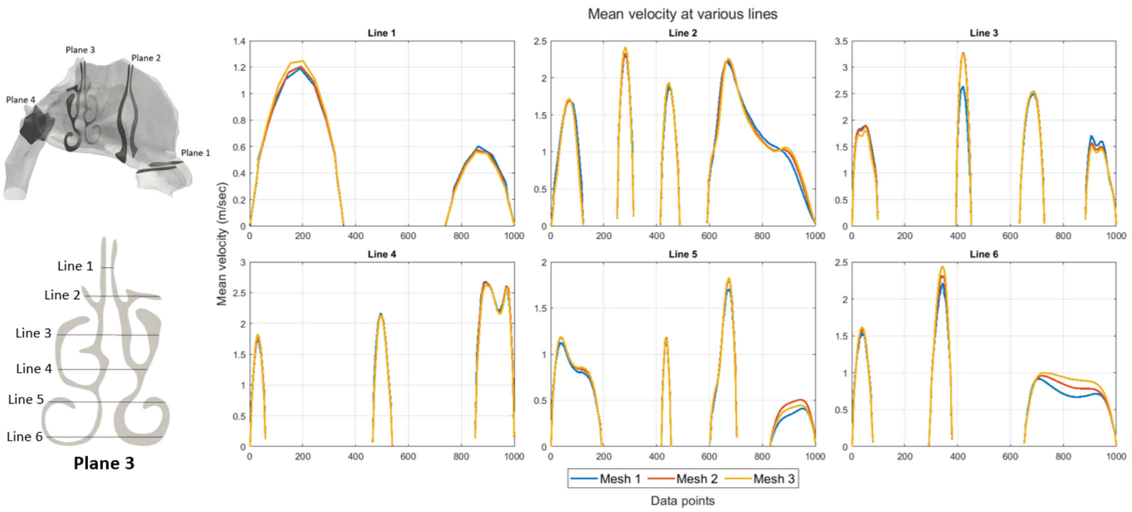

Figure 4.3: Line plots of mean velocity - plane 3.

left cavity, the difference is seen between these two meshes and mesh 1. On the contrary, there is a notable change in the mean velocity profile on line 4. The values on mesh 1 are different from that obtained on mesh 2 and 3. The velocities are not exactly similar for mesh 2 and 3, however, the nature of the mean velocity profile is alike.

In figure 4.3, mean velocity do not change much on all three meshes. Plane 4 is positioned near the nasopharynx, as seen in figure 4.4. The mean velocity profile on this plane shows that we get nearly similar results from mesh 2 and 3, and it differs from mesh 1, particularly on lines 1 and 2.

It is advantageous to study the mesh convergence on multiple planes as highlighted above. By doing this, it is ensured that the regions of poor mesh convergence are not neglected. From the study on this nasal cavity model, it is observed that the velocity profiles on mesh 1 were dissimilar to the results obtained on the other two meshes.

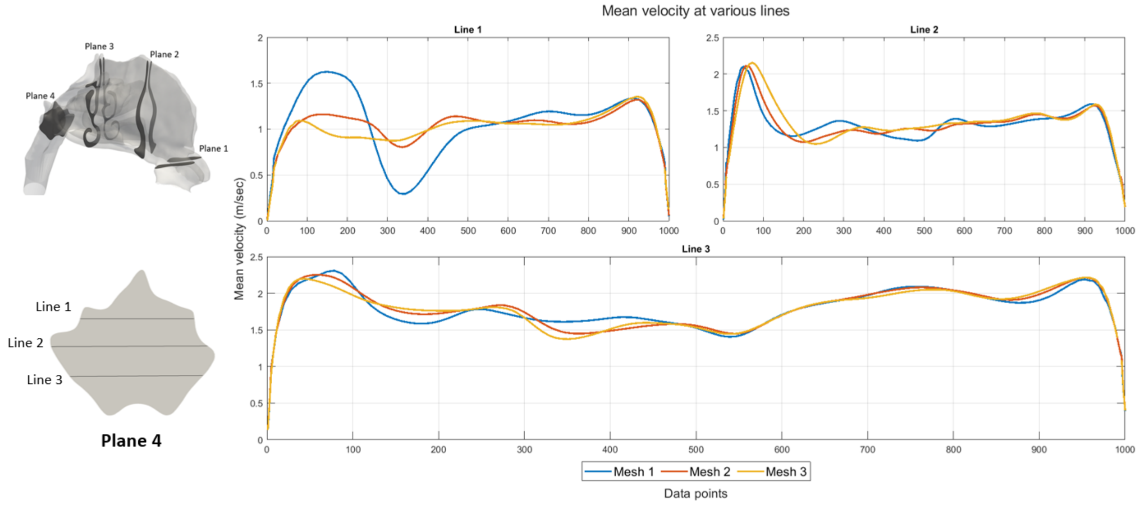

Figure 4.4: Line plots of mean velocity - plane 4.

Conversely, the results do not change much when the mesh is refined from mesh 2 to mesh 3. Hence, it can be concluded that it is beneficial to consider mesh 2 for simulations since the gain in the accuracy of the solution is insignificant compared to the increased computational time when using mesh 3. The final mesh at several coronal cross-sections along the nasal cavity are shown in figure 4.5.

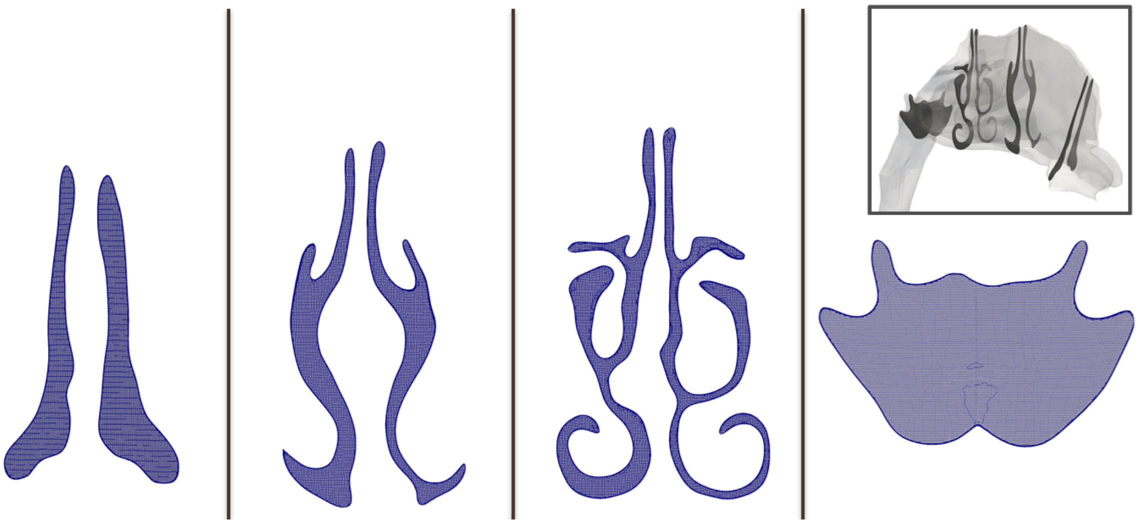

Figure 4.5: Computational mesh for model 1 at several coronal slices. In box: Location of the coronal slices in the nasal cavity.

4.1.2 Model 2

For analyzing the mesh, pressure drop at probe locations were compared to the experimental and CFD values from Strien *et al.*, see figures 4.6-4.8. A good agreement in experimental and CFD values was achieved from this study. The pressure distribution obtained using CFD in Strien *et al.* and the current mesh are very close to each other for all three flow rates.

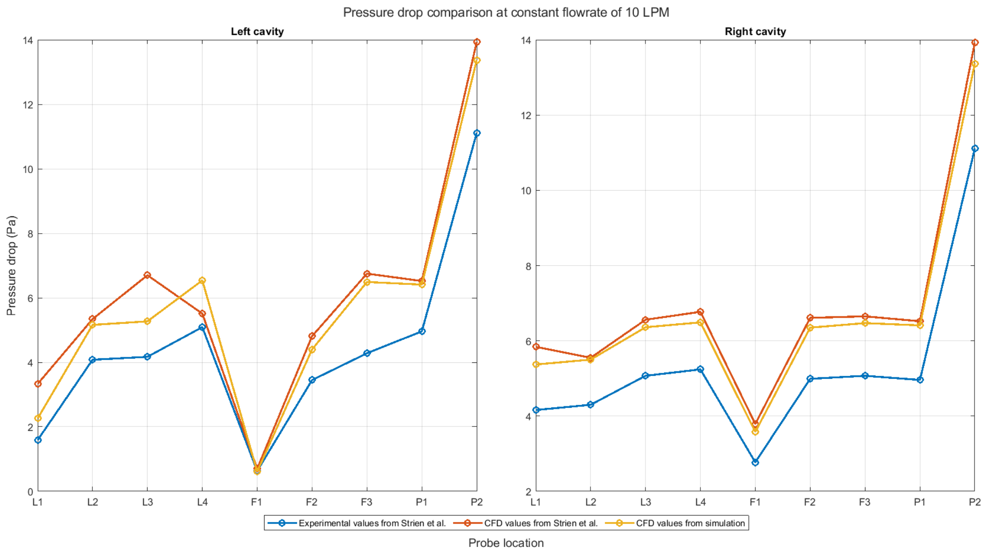

Figure 4.6: Comparison of pressure drop at constant flowrate of 10 LPM.

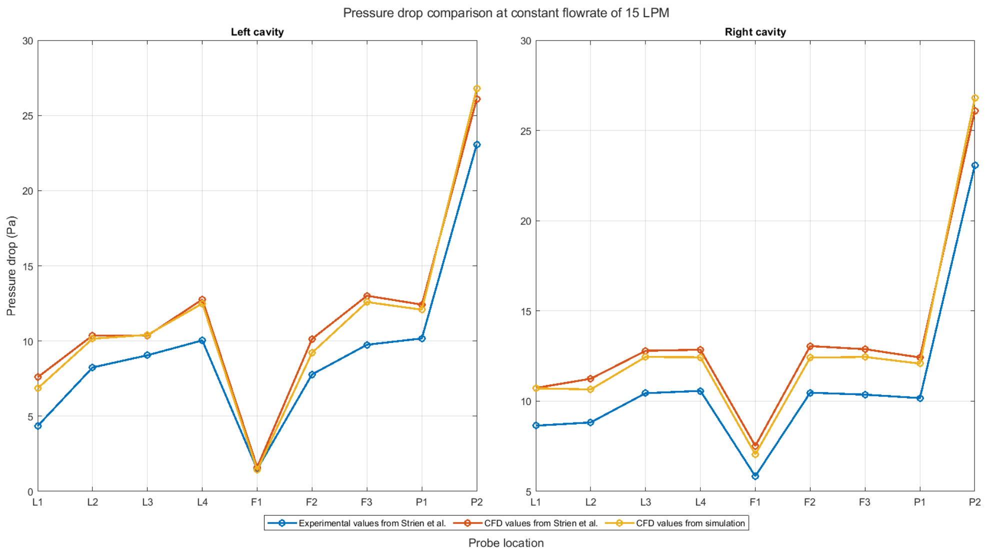

Figure 4.7: Comparison of pressure drop at constant flowrate of 15 LPM.

Additionally, velocity vectors at time $t = 0.2$ seconds and the mean velocity contours were compared for the 30 LPM flow rate case. The corresponding images are shown in Appendix B. By observing the flow vectors and the contours, the current mesh can reproduce the dominant features like recirculating regions and mixing flow streams. Therefore, it can be concluded that the mesh resolution is sufficient, and the results from Strien *et al.* can be replicated using this mesh.

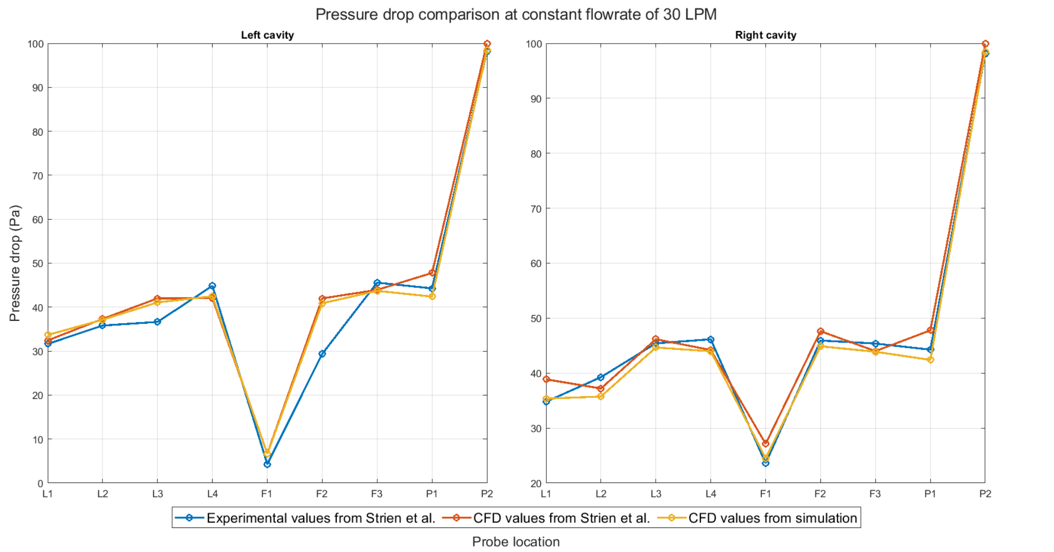

Figure 4.8: Comparison of pressure drop at constant flowrate of 30 LPM.

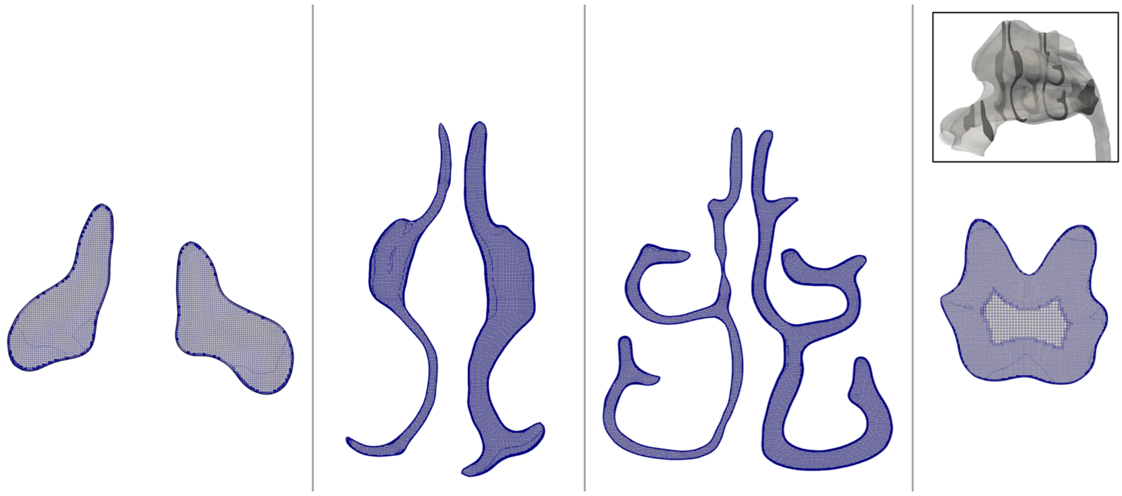

Figure 4.9: Computational mesh for model 2 at several coronal slices. In box: Location of the coronal slices in the nasal cavity.

4.2 Comparison between simulation and in-vitro pressure measurements

Figures 4.10-4.13 shows the pressure distribution at several probe locations in the right and left cavity of the nasal model. The study is performed for two mean flow rate cases - 15 LPM and 25 LPM (refer figure 3.13 for flow curve) on nasal cavity model 2. The location of the probes is discussed in the previous section (figure 3.9).

Case - 25 LPM mean flow rate

There is a good agreement in the pressure drop obtained from the experiments and the simulation in the right cavity, as seen from figure 4.10. Although the pressure

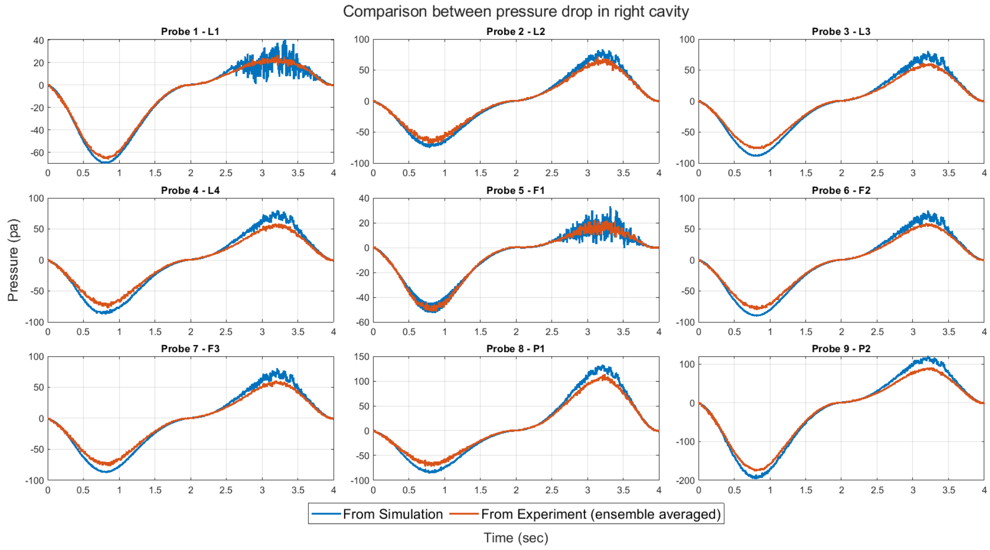

Figure 4.10: Comparison of pressure drop between simulation and experiments in right cavity - for a mean flow rate of 25 LPM.

magnitude does not match exactly, the trend exhibited during the tidal breathing cycle is the same in both cases. The pressure fluctuations which exist majorly during the exhalation period are captured in the simulation as well. The fluctuations are higher at probe F1 and L1, located just before and after the nasal valve region.

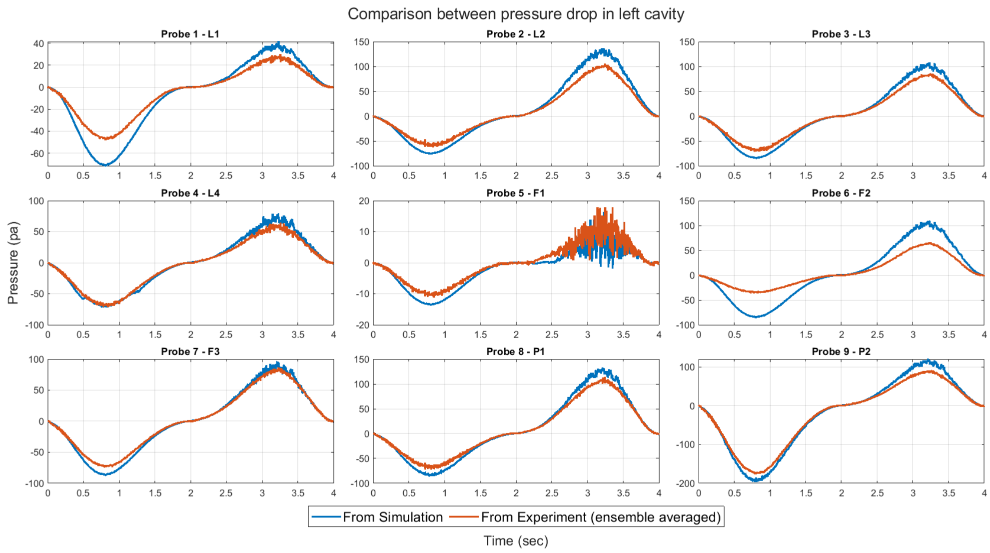

Figure 4.11: Comparison of pressure drop between simulation and experiments in left cavity - for a mean flow rate of 25 LPM.

Figure 4.11 gives the pressure distribution in the left cavity. The simulation results match well with the experiments, and the trends are reproduced effectively as well. However, for probe F2, the simulation data is dissimilar from the experimental results. It was because of leakage near the probe location. During the process of drilling the holes for the probes, the drill went a bit far, thus creating a hole opposite to the probe location. During the experiments, we tried to cover the hole with surgical tape, but due to the complex geometry of the 3D-printed model, it was not possible to completely seal it, and the effect of that can be seen in the pressure measurements at that location.

Case - 15 LPM mean flow rate

As observed from figure 4.12 and figure 4.13, the pressure drop from simulation agrees with the in-vitro experiments. The curves exhibit a similar trend to the 25 LPM case, except that the values of pressure are lower in magnitude.

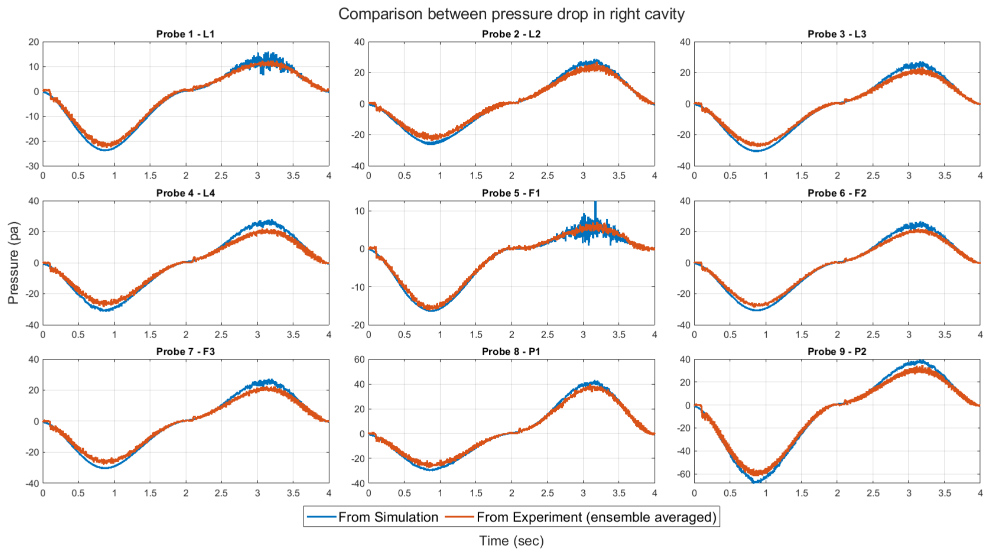

Figure 4.12: Comparison of pressure drop between simulation and experiments in right cavity - for a mean flow rate of 15 LPM.

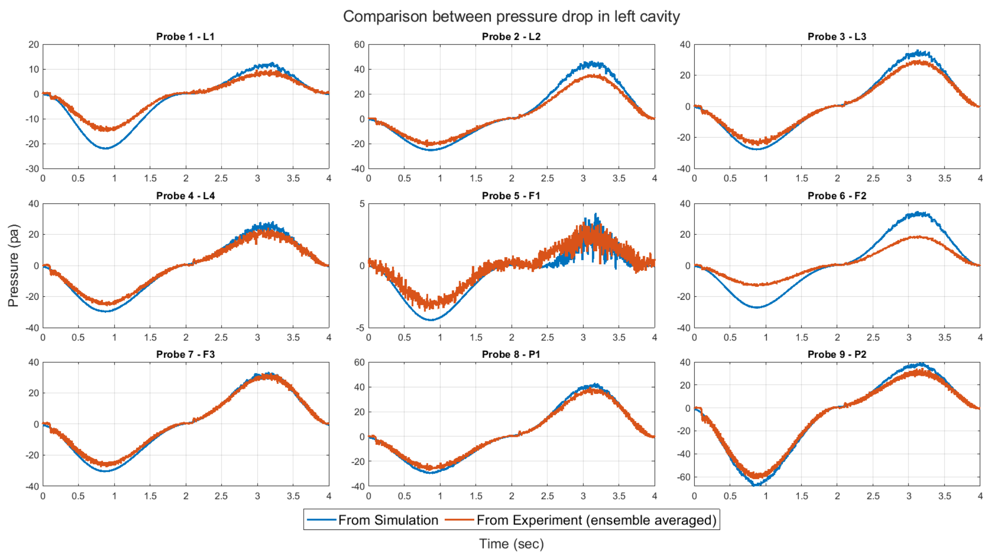

Figure 4.13: Comparison of pressure drop between simulation and experiments in left cavity - for a mean flow rate of 15 LPM.

In this study, the results indicate that the pressure distribution obtained by CFD simulations are slightly over-estimated. However, it should also be noted that the pressure drop values from experiments is not ideal, and there could be some pressure loss arising in the tubes connecting the probe and the device or due to leakages. Thus, it is inferred that the CFD simulations are capable of generating the solution of flow field with a reasonable accuracy.

The pressure measurements were also performed by blocking the left and right cavities simultaneously. It corresponds to how the rhinomanometry experiments are performed. Figure 4.14 and figure 4.15 show the pressure drop comparison in the blocked cavity for several probes during experiment and simulation. The results correspond to the 25 LPM mean flow rate case through the nasal cavity.

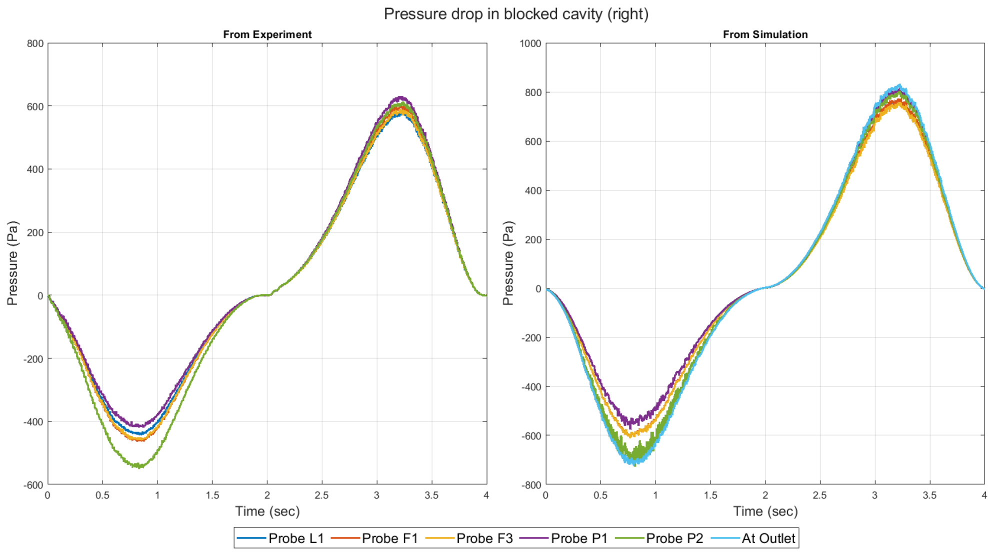

Figure 4.14: Pressure distribution at probe locations when right cavity is blocked.

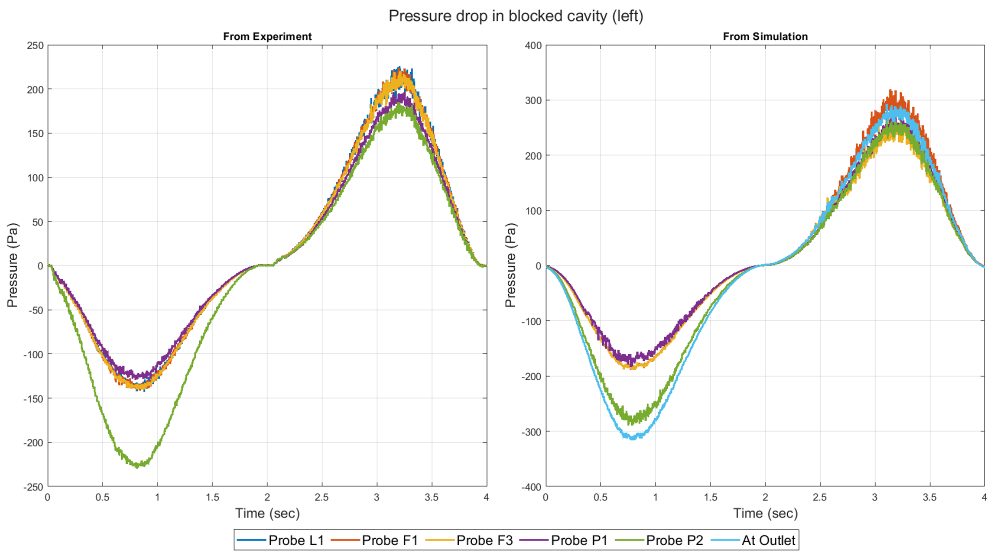

Figure 4.15: Pressure distribution at probe locations when left cavity is blocked.

The highest pressure drop during the inhalation period is observed at probe P2, located after the nasopharynx bend and close to the outlet. The pressure drop is similar and does not change significantly for the rest of the probe locations, which are situated anterior to the nasopharynx bend. This can be due to negligible flow in the blocked side of the nasal cavity. From these results, it is apparent that the large pressure drop is due to the sudden change in cross-sectional area along with the sharp bend at the nasopharynx. Although, the pressure drop during the exhalation period does not differ significantly from each other as it does during inhalation. Hence, to calculate the CFD-derived nasal resistance, pressure drop values before the nasopharynx bend should also be considered and compared with the rhinomanometry experiments.

4.3 Comparison between simulation and in-vitro rhinomanometry

In this section the nasal resistance values derived from CFD simulation are compared with the measurements obtained by in-vitro rhinomanometry.

4.3.1 Model 1

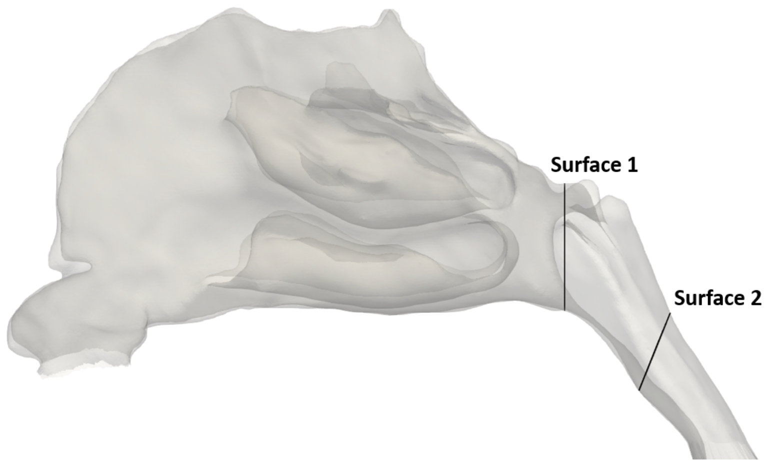

Figure 4.16: Location of plane for rhinomanometry measurement - model 1.

The CFD-derived nasal airway resistance is typically calculated based on the pressure-flow curves at the outlet of the nasal model. In the rhinomanometry experiment, it was assumed that the pressure near the nostril in the blocked cavity, where the probe of the rhinomanometer lies, is equal to the pressure at the nasopharynx. However, when one nostril is blocked, we have seen that the pressure varies drastically in the nasopharynx due to the reduction in cross-sectional area and the sudden bend. Due to this, it is apparent that the pressure-flow curves will differ based on the location of the plane where the pressure is measured during the simulations. Therefore, in addition to the outlet, nasal resistance is calculated on two additional planes as defined in figure 4.16. The advantage of using CFD is that the pressure-flow curve can be defined at any location inside the nasal cavity.

Table 4.1: Nasal airway resistance - model 1.

Model	**Mean flow rate**	**Method**	**Location on probe/plane for pressure drop measurement**	**NAR Left cavity** ($Pa/cm^3/sec$)	**NAR Right cavity** ($Pa/cm^3/sec$)	**NAR Total nose** ($Pa/cm^3/sec$)
Model 1	15 LPM	Experiment	Nostril	0.118	0.088	0.052
		Simulation	Outlet	0.071	0.057	0.023
			Surface 1	0.068	0.054	0.020
			Surface 2	0.069	0.055	0.021

Table 4.1 presents the CFD-derived nasal resistance for the left cavity, right cavity, and total nose. From the experimental results, it is concluded that the nasal cavity model is not experiencing any obstructions. The CFD-derived nasal resistance obtained at the outlet is similar to the nasal resistance from surfaces 1 and 2. The results from simulation and experiments do not correlate significantly. However, the values can be said to be close to each other, considering the lower nasal resistance in the cavity.

4.3.2 Model 2

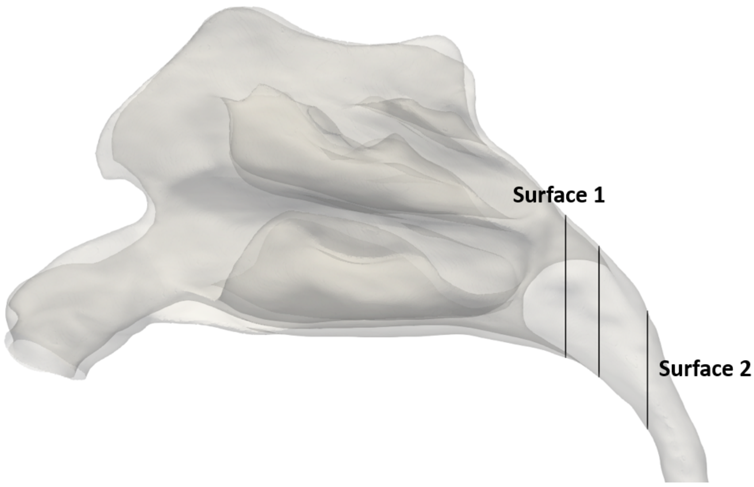

Figure 4.17: Location of plane for rhinomanometry measurement - model 2.

Similar to model 1, additional planes are defined to evaluate the pressure-flow curves. Figure 1 depicts the location of these planes. The mean flow rate curves corresponding to 15 and 25 LPM were used in the simulation.

Table 4.2: Nasal airway resistance - model 2.

Model	**Mean flow rate**	**Method**	**Location on probe/plane for pressure drop measurement**	**NAR Left cavity** ($Pa/cm^3/sec$)	**NAR Right cavity** ($Pa/cm^3/sec$)	**NAR Total nose** ($Pa/cm^3/sec$)
Model 2	15 LPM	Experiment	Nostril	0.350	0.127	0.103
		Simulation	Outlet	0.351	0.140	0.094
			Surface 1	0.305	0.085	0.042
			Surface 2	0.314	0.101	0.054
Model 2	25 LPM	Experiment	Nostril	0.368	0.146	0.091
		Simulation	Outlet	0.386	0.152	0.101

The CFD derived nasal resistance at outlet is similar to the one obtained from the rhinomanometry experiments for both the flow rate case, as seen in table 4.2. The resistance values at surfaces 1, 2, and 3 are lower than the nasal resistance at the outlet. This is similar to what was observed in model 1. Although a statistical significance could not be established, the CFD-derived nasal resistance observed at the outlet lies in the 95% reference interval range of the experimental values.

The experimental, as well as the nasal resistance at the outlet for the left cavity, right cavity, and total nose, are similar for both the flow rate cases. It suggests that the value of peak and mean flow rate for a breathing profile does not considerably influence the nasal resistance. Hence, even if the tidal breathing profile of humans varies during consecutive rhinomanometry measurements, it rarely will affect the nasal resistance value.

4.4 Tidal breathing

The results from the tidal breathing simulation performed on both the nasal cavity models are discussed in this section. The images presented in this section corresponds to the tidal breathing simulation performed at a mean flow rate of 15 LPM.

4.4.1 Model 1

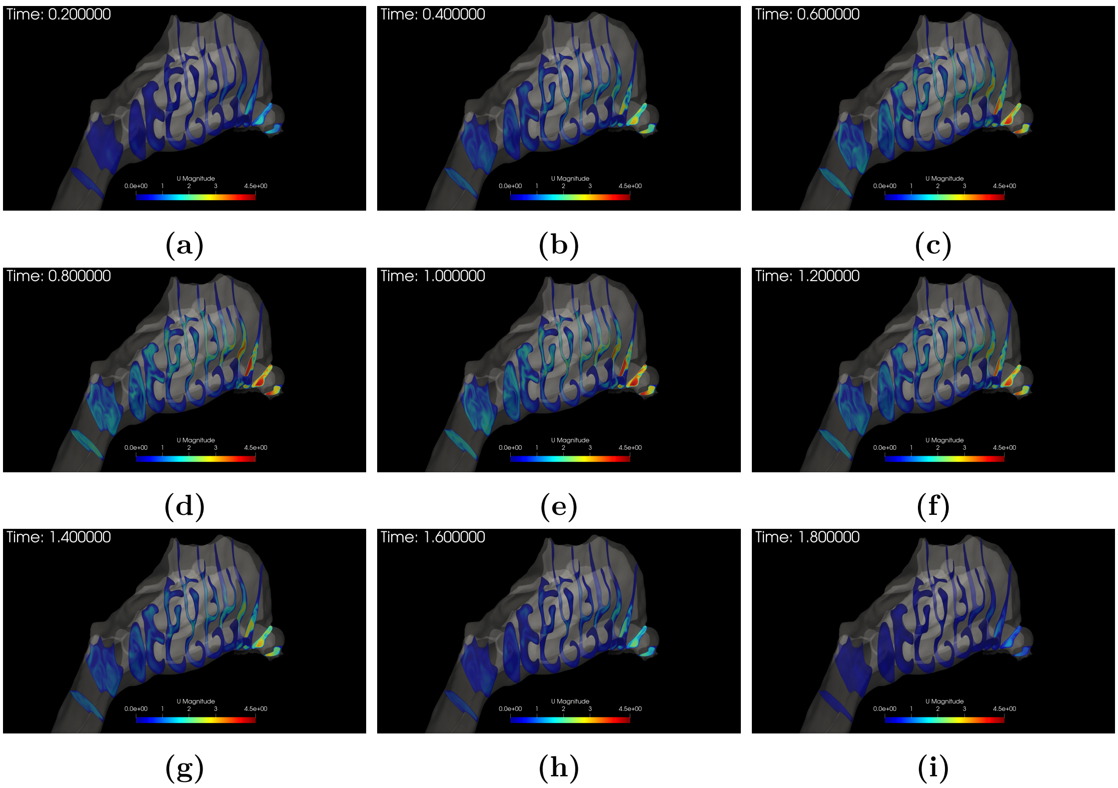

Figure 4.18: Velocity contour in right cavity during inhalation - model 1.

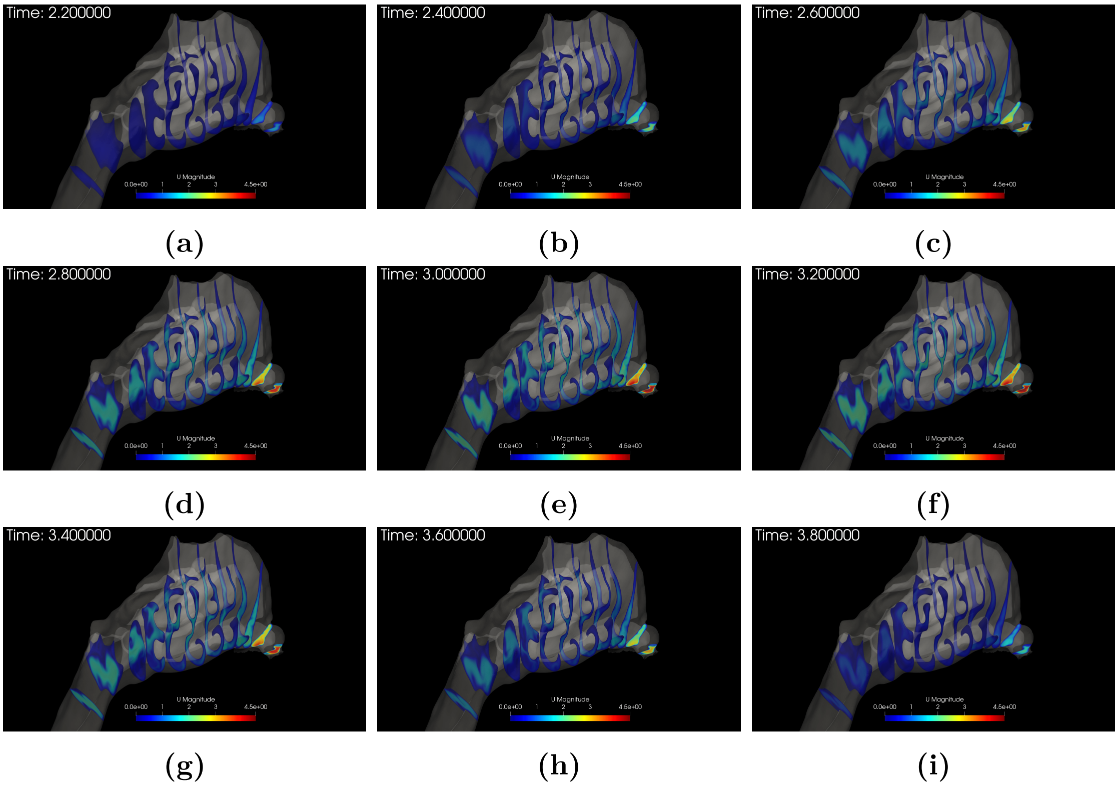

Figure 4.19: Velocity contour in right cavity during exhalation - model 1.

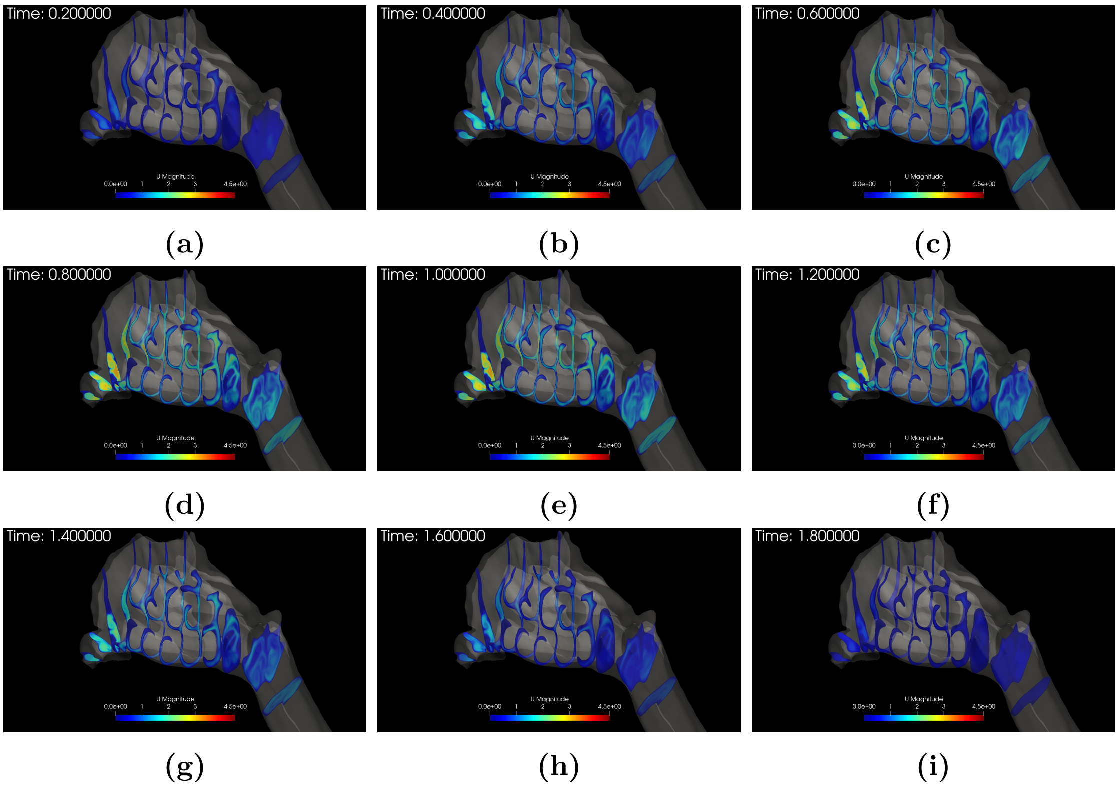

Figure 4.20: Velocity contour in left cavity during inhalation - model 1.

The airflow in the nasal passage is visualized by plotting the velocity contours at several coronal slices. Figure 4.18 and figure 4.19 shows the velocity in the right nasal passage during inhalation and exhalation respectively.

During inhalation, higher velocities are observed near the nostril as well as at the nasal valve region. The flow is uniform in the inferior portion of the nasal vestibule while unsteady, disturbed flow can be seen in the superior portion. This is due to the encounter of incoming air with the notch present in the nasal cavity. In the respiratory region, the velocity decreases as the cross-sectional area increases, and the incoming air diffuses into the inferior, middle, and superior meatus. A large volume of flow exists in the superior part of the respiratory region and close to the septum wall, whereas a relatively low amount of air passes through the floor of the nasal cavity. At the posterior of the nasal cavity where the two chambers merge, an unsteady flow and formation of small vortexes can be observed. This is due to the mixing of air streams from the right and left nasal cavities.

During exhalation, owing to the small cross-sectional area after the nasopharynx bend, the air enters the nasal passage in the form of a jet. Similar to the inhalation period, as the flow splits into individual cavities, a majority of the air flows from the passage close to the septum wall as well as the meatuses. There is slightly more flow in the floor of the nasal cavity compared to the inhalation period. Hence, the velocity in the meatus and near the septum wall decreases minutely. The velocity increases in the nasal vestibule and near the nostril as air is exhaled from the nose.

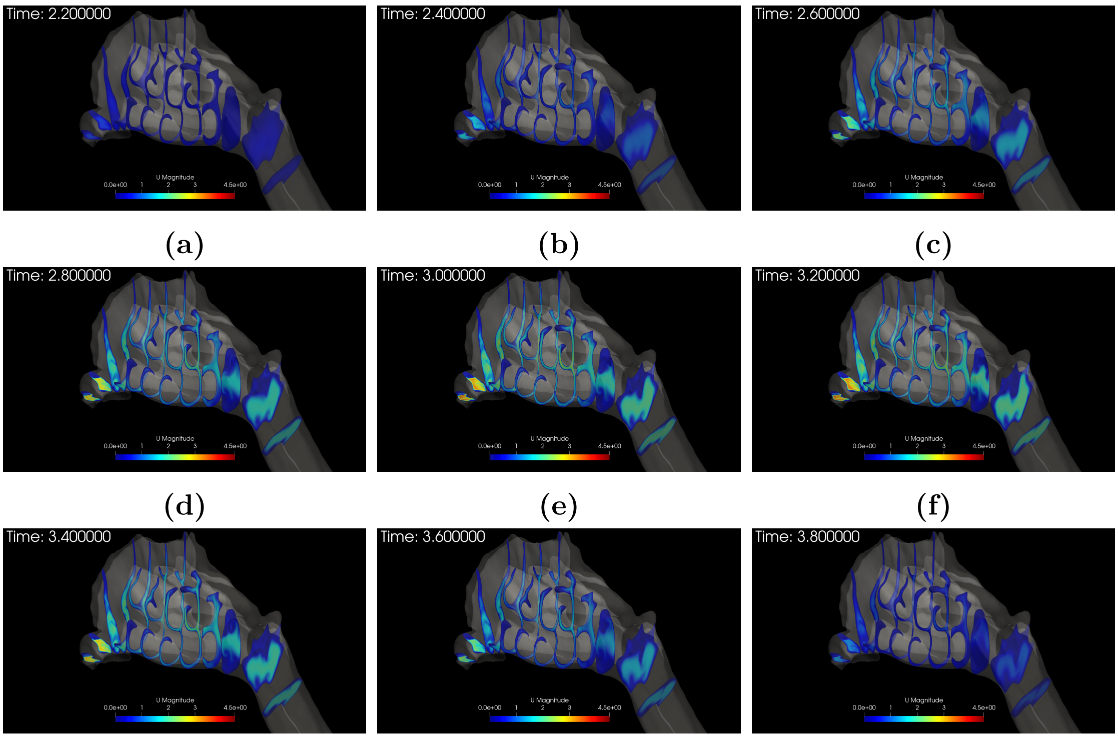

(a) (b) (c)

(d) (e) (f)

(g) (h) (i)

Figure 4.21: Velocity contour in left cavity during exhalation - model 1.

Figures 4.20 and 4.21 presents the velocity contours in the left cavity during inhalation and exhalation respectively. The left nasal cavity appears to be a bit smaller in cross-section compared to the right cavity. This is because of the nasal cycle phenomena. The flow is uniform in the nasal passage, and more amount of air is seen to pass through the nasal cavity floor. However, at the nasal vestibule and the nasopharynx region, the overall trends viewed for the left cavity during the inhalation and exhalation period are similar to the right cavity.

4.4.2 Model 2

The airflow during the inhalation period can be visualized by examining the velocity contours at several coronal planes in the right cavity as shown in figure 4.22. The flow is uniform as it enters the nostril, and it continues in the nasal vestibule with small disturbances. A small vortex starts to develop in the inferior side, probably due to the geometry variation as the cross-sectional area reduces from the nasal vestibule to the nasal valve region. After the nasal valve region, the flow is accelerated due to a reduction in cross-sectional area. There is no significant flow in the olfactory region during the inhalation period as most of the flow passes along the septum wall, the middle meatus, and the floor of the nasal cavity.

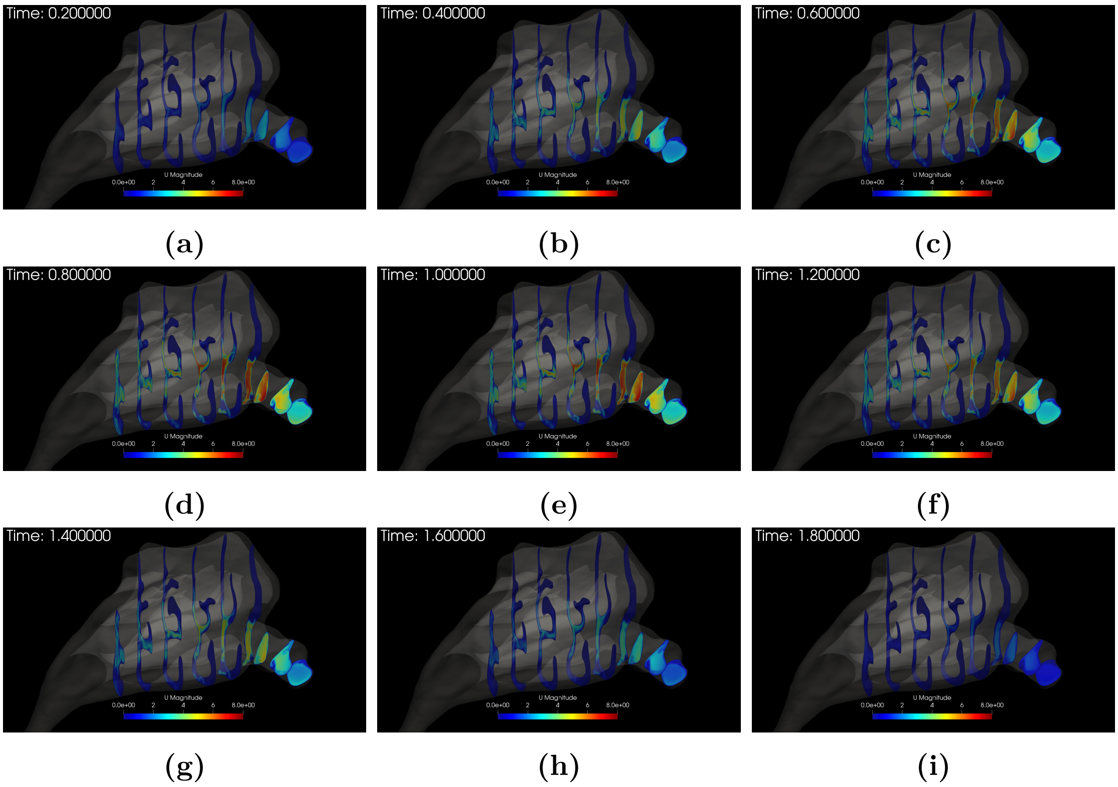

(a) (b) (c) (d) (e) (f) (g) (h) (i)

Figure 4.22: Velocity contour in right cavity during inhalation - model 2.

In figure 4.23, the velocity contours in the right cavity during the exhalation period are shown. The path followed by air during exhalation is significantly different from that observed during the inhalation period. A majority of air seems to pass through the olfactory region, located at the top of the nasal cavity. Compared to

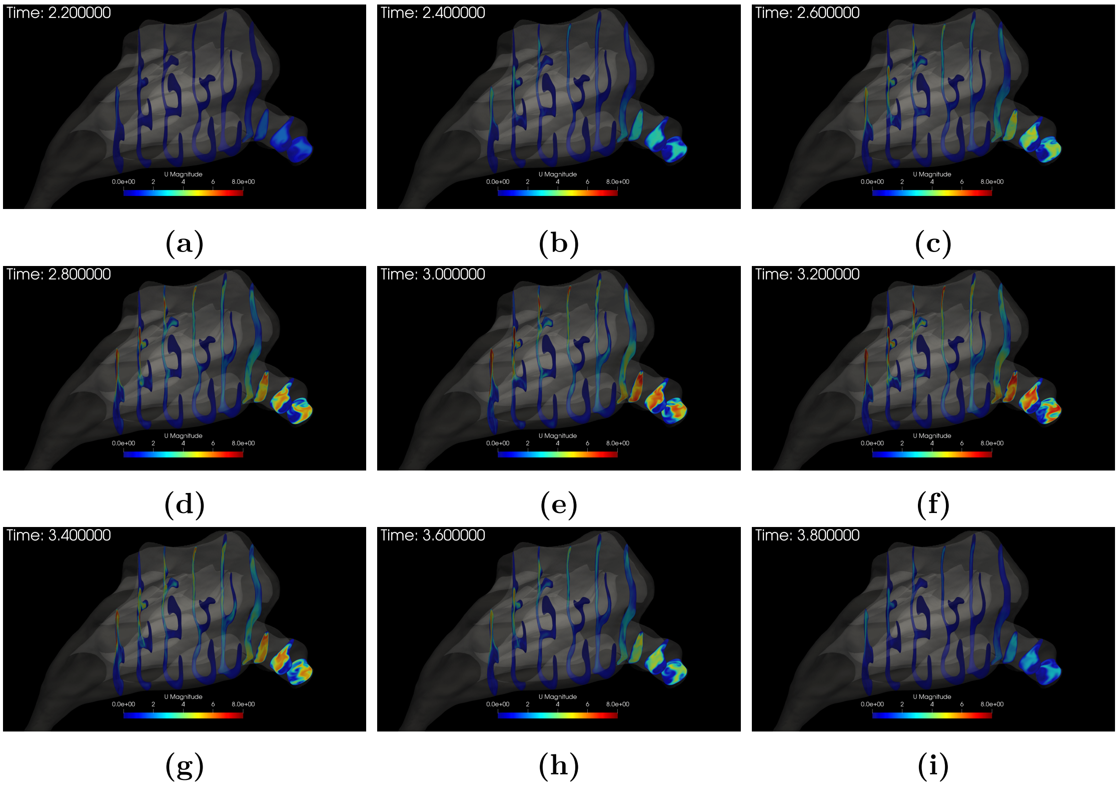

Figure 4.23: Velocity contour in right cavity during exhalation - model 2.

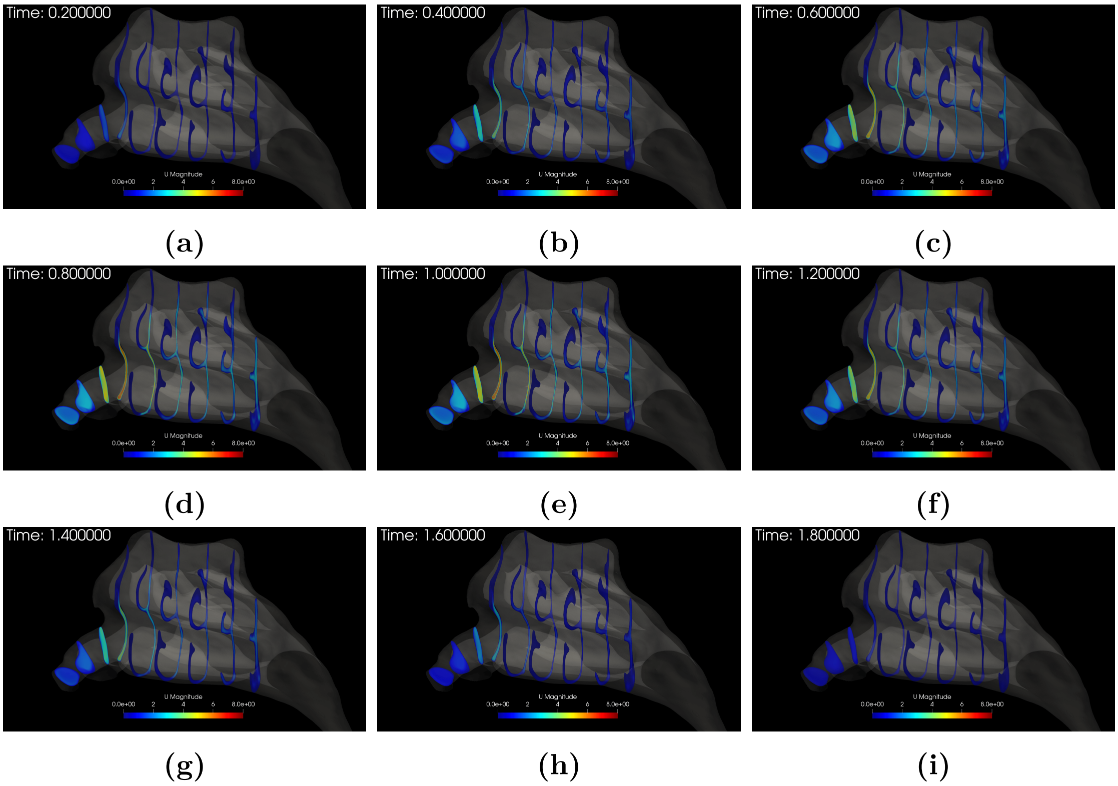

Figure 4.24: Velocity contour in left cavity during inhalation - model 2.

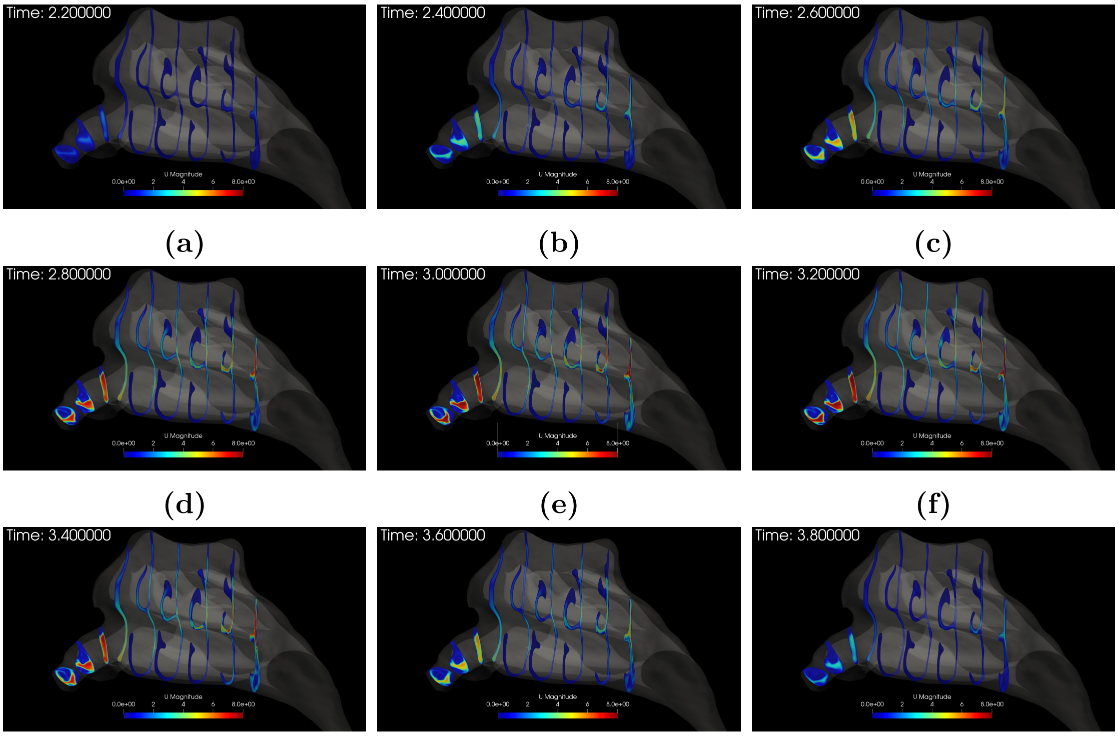

(a) (b) (c) (d) (e) (f) (g) (h) (i)

Figure 4.25: Velocity contour in left cavity during exhalation - model 2.

the inhalation period, the airflow along the septum wall and middle meatus have decreased during exhalation. A negligible amount of flow is seen at the floor of the cavity and in the inferior meatus. The nasal vestibule region has a very disturbing airflow due to geometric changes and a sudden expansion after the nasal valve region. The velocities observed during exhalation are higher compared to the inhalation period. This is due to the high velocity jet coming from the narrow section after the nasopharynx bend.

Figure 4.24 and 4.25 shows similar velocity contours in the left cavity during inhalation and exhalation period respectively. The cross-sectional area in the left cavity is significantly smaller as compared to the right side. This is the reason for a notable difference in nasal resistance observed in both the cavities. Due to a smaller area and a high resistance to the flow, we see a more uniform airflow in the left cavity. However, the trends during inhalation and exhalation are similar in both cavities.

4.5 Steady state solution .vs. tidal breathing simulation

To examine whether the quasi-steady assumption for nasal airflow accurately replicates the results of a tidal breathing simulation, the steady-state solution is compared with the tidal breathing simulation results. The comparison is done for flow rate corresponding to two instants each during inhalation ($t = T_1$ and $t = T_2$) and exhalation period ($t = T_3$ and $t = T_4$) as indicated in figure 4.26. The time instances for comparison are selected such that they are just before and after the peak flow during inhalation as well as exhalation.

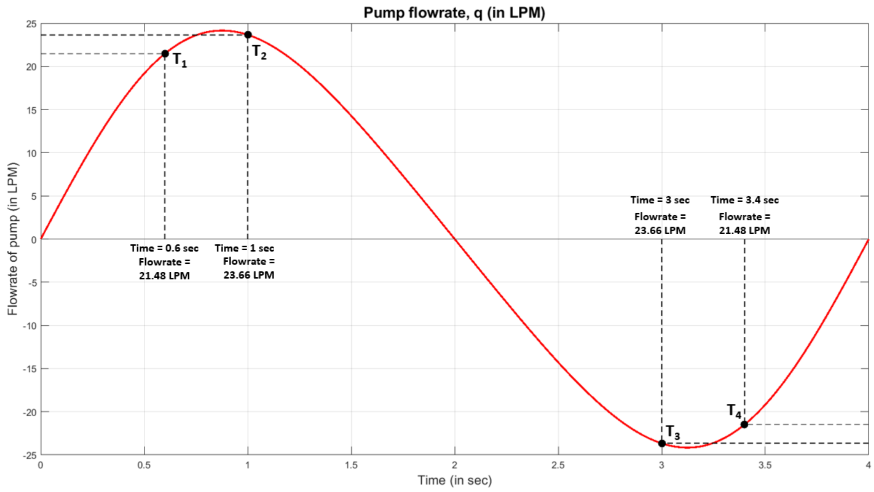

Figure 4.26: Instances of time selected for comparison with tidal breathing simulation.

4.5.1 Comparison of mean velocity contours

Figures 4.28-4.29 shows the mean velocity contour at several planes inside the nasal cavity. The comparison between the tidal breathing simulation result and steady-state solution is made by observing these contours at certain time instances as described in figure 4.26.

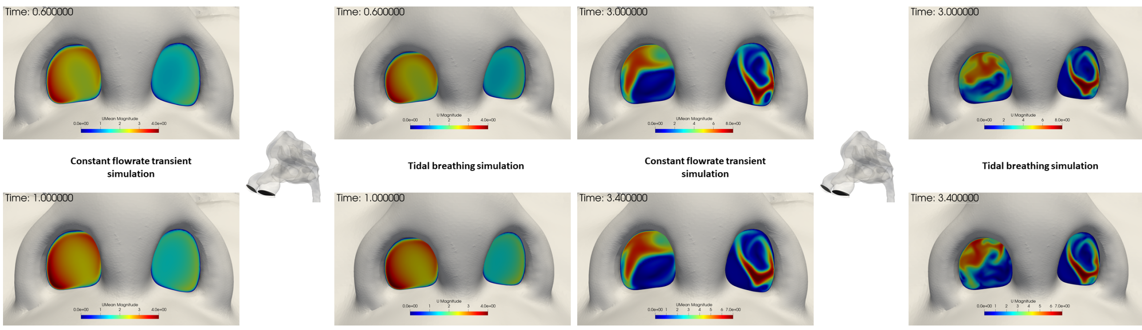

(a) (b)

Figure 4.27: Mean velocity contour near nostrils.

A notable difference in the velocity contours of steady-state solution and tidal breathing simulation during the exhalation phase is also observed at a plane near the nostrils, as seen in figure 4.27. From figure 4.28, the velocity contour during the inhalation phase appears to be similar as the vortexes and flow structures are accurately captured in steady-state solution as well. However, a significant difference can be observed during the exhalation phase even if the flow rate is the same in both cases. The flow field in tidal breathing simulation is unsteady, and a significant amount of flow exists in inferior turbinate. The velocity contour for the steady-state solution appears to be smeared out and remarkably different than the tidal breathing result. The local unsteadiness is not observed and, the flow seems to be absent in the inferior turbinate as well.

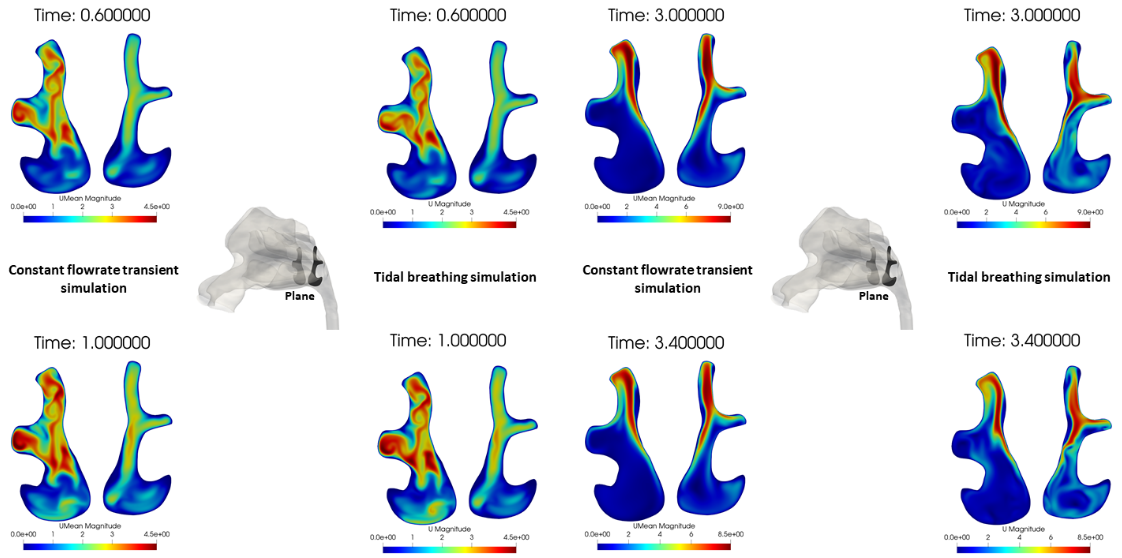

(a) (b)

Figure 4.28: Mean velocity contour at a coronal plane in posterior of the cavity.

Similar observations can be made by analyzing the mean velocity contour in the right cavity given in figure 4.29. The overall flow features are replicated in the steady-state solution during inhalation. However, the inertial effect in exhalation seems to be more prominent, and the effect of this is not captured in the steady-state solution during exhalation period. The vortexes formed due to mixing if air from two cavities at the nasopharynx section are not seen in the steady-state solution during exhalation. These observations are consistent and can be seen by studying the velocity contours at several other planes in the nasal cavity, additional results are presented in Appendix C.

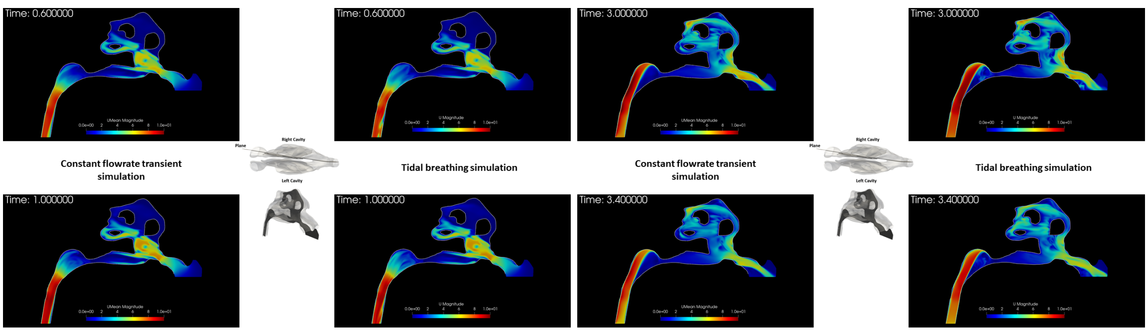

(a) (b)

Figure 4.29: Mean velocity contour at a sagittal plane in right cavity.

4.5.2 Comparison of pressure distribution in the nasal cavity

The differences in steady-state solution and tidal breathing results are further analyzed by studying the pressure distribution inside the nasal cavity.

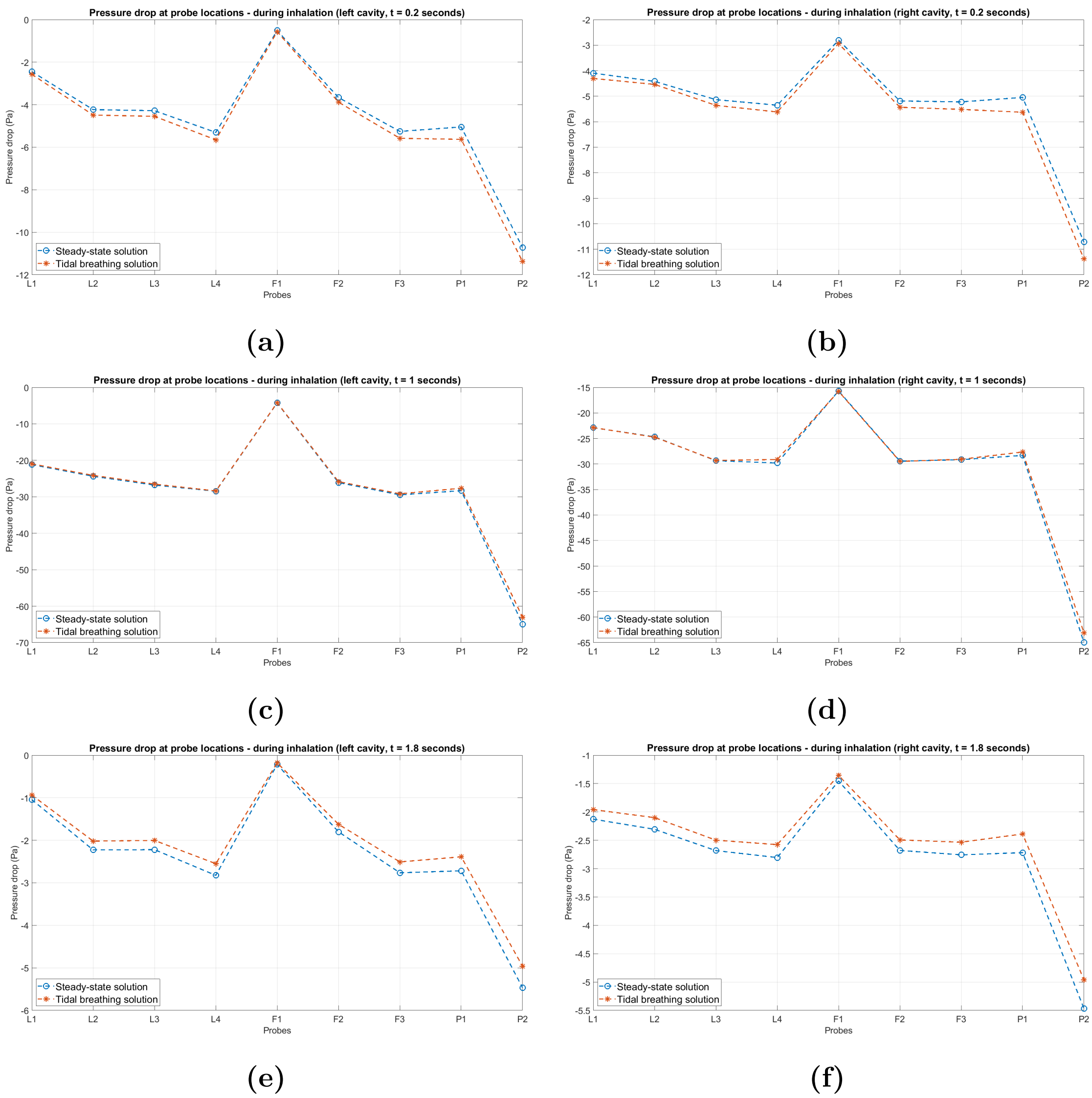

Figure 4.30: Comparison of steady-state and tidal breathing pressure drop during inhalation phase.

Figure 4.30 and figure 4.31 compares the pressure drop at probe locations (depicted in figure 3.9) during inhalation and exhalation phase respectively. During inhalation, the pressure drop values from steady-state solution and tidal breathing simulation are similar. However, at high flow rates (t = 3 seconds) during exhalation, the pressure drop obtained from the steady-state solution does not match with tidal breathing results. Thus, it is established again that the steady-state solution during the exhalation period cannot imitate the tidal breathing simulation results.

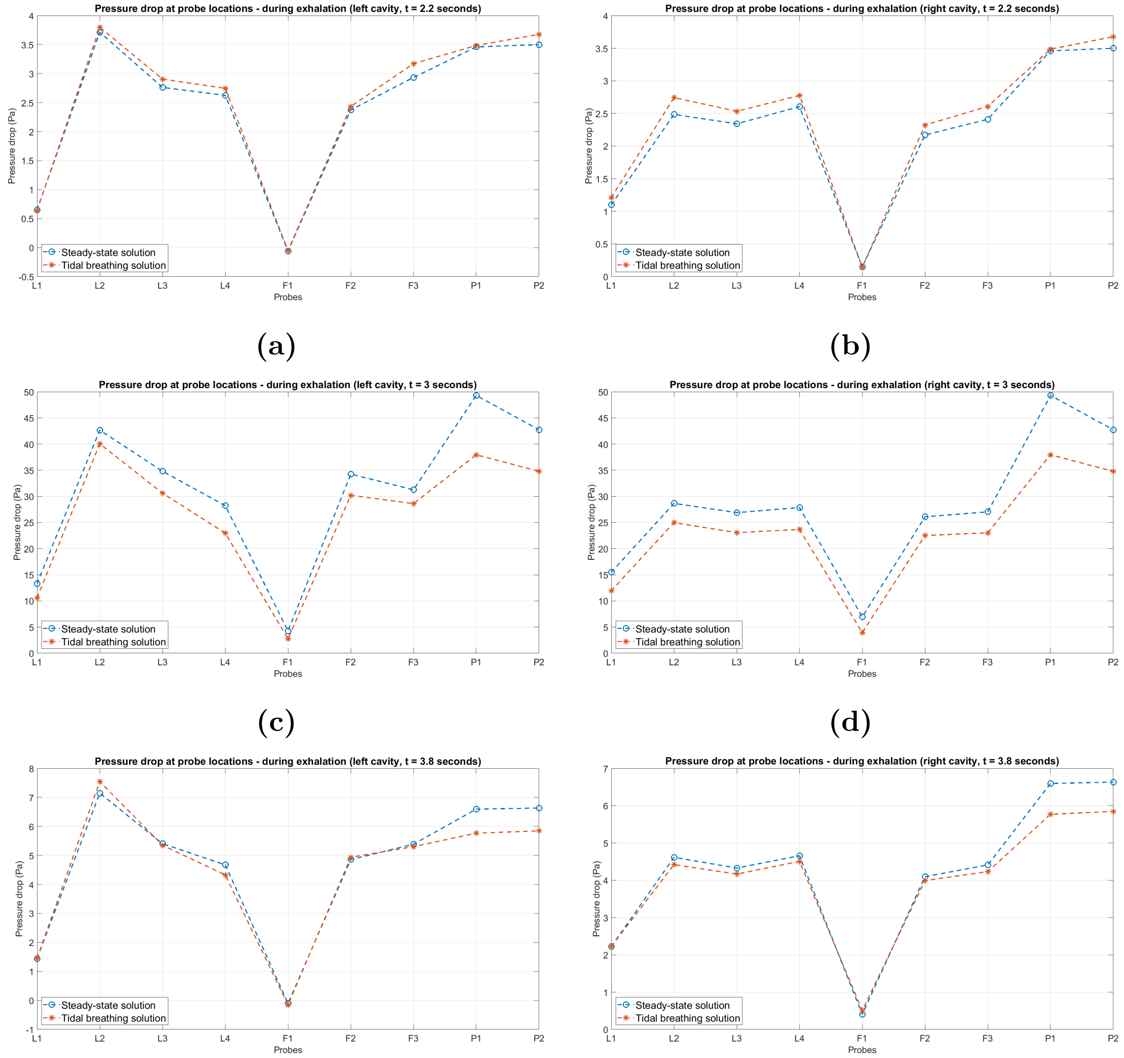

(a) (b) (c) (d) (e) (f)

Figure 4.31: Comparison of steady-state and tidal breathing pressure drop during exhalation phase.

4.5.3 Comparison of nasal resistance

The pressure-flow curve required to calculate the nasal resistance can be constructed based on the steady-state results. A fitted curve is drawn using the values of pressure and flow rate obtained from steady-state solutions at several time instances along the flow curve. The nasal resistance for the steady-state results are then calculated based on this curve. Figure 4.32 shows the fitted pressure-flow curve which is drawn based on the steady-state results at several flow rate boundary condition.

Table 4.3 shows how the nasal resistance obtained from steady-state solution compares with the tidal breathing and experimental nasal resistance. It is seen that the fitted pressure-flow curve can provide similar nasal resistance values compared to tidal breathing simulation. Thus, it can be concluded that steady-state solutions can be used to accurately calculate the nasal resistance instead of the computationally

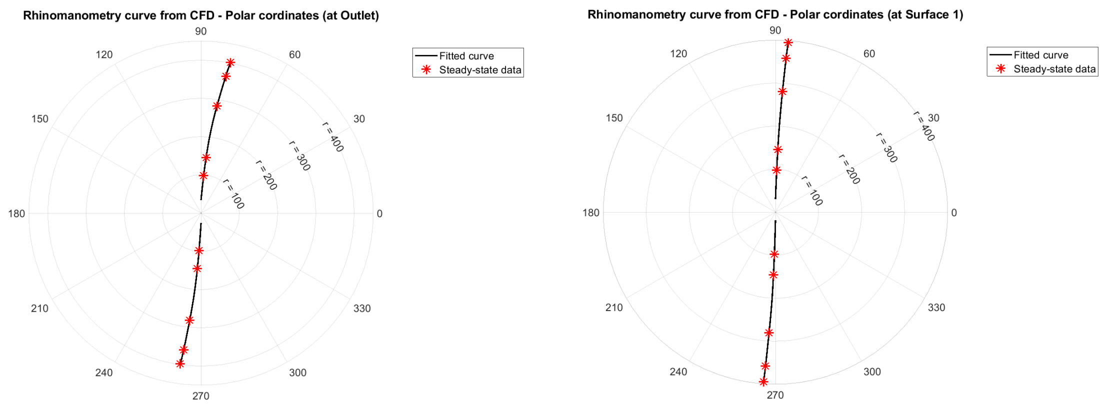

(a) **(b)**

Figure 4.32: Pressure-flow curve from steady-state results.

expensive tidal breathing simulations.

Table 4.3: Nasal airway resistance - comparison of tidal breathing and transient constant flow rate simulation.

Model	**Mean flow rate**	**Method**	**Location on probe/plane for pressure drop measurement**	**NAR Total nose (Pa/cm3/sec)**
Model 2	15 LPM	Experiment	Nostril	0.103
		Simulation - Tidal breathing	Outlet	0.094
			Surface 1	0.042
			Surface 2	0.054
		Simulation - Transient constant flow rate	Outlet	0.097
			Surface 1	0.042
			Surface 2	0.055

5

Conclusion

In this project, an effort was made to understand the flow inside a human nasal cavity model under tidal breathing using the CFD technique. The notable outcomes from this study are discussed further in this section.

The CFD methodology used in this project provided a sufficiently accurate solution. The pressure distribution in the nasal cavity obtained during experiments was similar to the results obtained from CFD simulations. It was inferred that the simulations can accurately predict the flow characteristics in a complex nasal cavity geometry during a tidal breathing cycle.

Rhinomanometry is the current objective measurement tool that doctors use for diagnosing nasal obstructions. The pressure-flow curves obtained from in-vitro rhinomanometry can be replicated using the data obtained from CFD simulation. The nasal resistances derived from CFD simulations were similar in value to the one measured during rhinomanometry experiments. Thus, it was concluded that the tidal breathing simulation results are helpful to calculate the nasal airway resistance with sufficient accuracy.

The tidal breathing profile is unique for each individual. Hence, for the simulation of the nasal cavity of a particular patient, a correct flow curve must be specified. In this project, two flow curves with different mean and peak flow rates were used. The nasal airway resistances obtained using these flow curves were similar to each other. Thus, the influence of the absolute flow rate of the breathing profile is negligible on the nasal resistance of a particular cavity. Hence, as long as the main characteristics of the breathing profile are preserved, the nasal resistance values would not vary significantly. So, a breathing profile averaged out from several patient datasets could be used alternatively if the precise breathing profile of the patient is unavailable.

The possibility of replicating the tidal breathing results with a steady-state solution was evaluated. It was inferred that the flow field, as well as the pressure distribution in the nasal cavity during the exhalation period was not accurately calculated in the steady-state solution. The cyclic nature of the inspiration-expiration process manifests hysteresis, which the steady-state solution fails to capture. Thus, to precisely visualize the flow during the breathing cycle, a tidal breathing simulation is necessary as the inertial effects associated with an unsteady and cyclic flow are critical during the exhalation phase. However, the nasal resistance from steady-state solution was similar to the tidal breathing nasal resistance. For situations where the clinician is only interested to determine the nasal resistance and not the flow features inside the nasal cavity, steady-state simulations can be performed, which would save a lot of computation time.

It is concluded that CFD simulations are capable of predicting the flow characteristics as well as the resistance of the nasal cavity. With the help of the results obtained by CFD simulation, the airflow path during the inhalation and exhalation period can be easily visualized at any coronal or sagittal cross-section or any complex location in the nasal cavity. Furthermore, it was observed that the nature of flow inside the nasal cavity is not unique. It will vary for each individual depending on the nasal geometry. Hence, the doctor needs to study the flow inside the nasal passage of the patient before performing any surgery. The post-processing capabilities of a CFD simulation can enable the doctor to effortlessly visualize detailed flow parameters at various stages of the breathing cycle. The current objective methods are not capable of providing such detailed insights of the flow inside the nasal cavity. Thus it can be concluded that using CFD as a tool for diagnosing nasal obstructions would provide a plethora of information to the doctors for planning effective surgical procedures and increase the success rate of such surgeries.

5.1 Future work

In this project, the pressure distribution in the nasal cavity is compared to validate the CFD model. Additionally, Particle Image Velocimetry (PIV) experiments could be performed to compare the instantaneous velocity field from the simulations. It would help to gain confidence in the CFD methodology that has been established.

A study could also be performed to validate the virtual surgery procedure on the nasal model. Rhinomanometry can be performed before and after the surgery on the patient. The surgery performed on the patient could be replicated digitally on the nasal cavity model. The pre and post-operative (on modified nasal cavity model) CFD-derived nasal resistance then needs to be compared with the rhinomanometry measurements.

Once the virtual surgery process is validated, it could prove helpful to clinicians to diagnose nasal obstructions in patients. Pre-operative CFD analysis could be performed on the obstructed nasal cavity. It would give vital information to the clinician regarding the blockage inside the nasal passage. The 3D model of the nasal cavity can then be modified to imitate the surgery. Simulating the post-operative model will help the clinician to evaluate the effect of the surgical procedure.

A simplified sinusoidal breathing cycle was used in simulations and experiments due to time constraints. It is easy to incorporate a breathing cycle similar to that observed in humans while performing CFD simulations. A simple change in the boundary condition does the trick. However, the stepper motor needs to be extensively programmed to mimic such a breathing cycle in experiments. It would be interesting to compare the in-vitro and in-silico measurements when an actual tidal breathing cycle is employed in simulations and experiments. Using a patient-specific breathing flow curve will make the virtual surgery procedure more realistic.

A large sample size of patients is required to establish a statistical significance between the nasal resistance derived from CFD and rhinomanometry. In the future, by referring to the methodology developed in this project, several nasal cavity models can be analyzed to calculate and collect the nasal resistance values. A statistical study can then be performed to correlate rhinomanometry and CFD-derived nasal resistance.

Bibliography

[1] S.S. Davis and Ronald Eccles. "Nasal congestion: Mechanisms, measurement and medications. Core information for the clinician". In: *Clinical otolaryngology and allied sciences* 29 (Jan. 2005), pp. 659–66. DOI: 10.1111/j.1365-2273.2004.00885.x.

[2] Rakesh Kumar Chandra, Monica Oberoi Patadia, and Joey Raviv. "Diagnosis of Nasal Airway Obstruction". In: *Otolaryngologic Clinics of North America* 42.2 (2009). Surgical Management of Nasal Obstruction, pp. 207–225. ISSN: 0030-6665. DOI: https://doi.org/10.1016/j.otc.2009.01.004.

[3] Rhee J. S., Sullivan C. D., Frank D. O., Kimbell J. S., and Garcia G. J. "A systematic review of patient-reported nasal obstruction scores: defining normative and symptomatic ranges in surgical patients". In: *JAMA Facial Plast Surg* 16.3 (2014), pp. 219–225.

[4] S. S. Pawar, G. J. Garcia, J. S. Kimbell, and J. S. Rhee. "Objective measures in aesthetic and functional nasal surgery: perspectives on nasal form and function". In: *Facial Plast Surg* 26.4 (Aug. 2010), pp. 320–327.

[5] M. A. Burgos, M. A. Sevilla García, E. Sanmiguel Rojas, C. Del Pino, C. Fernández Velez, F. Piqueras, and F. Esteban Ortega. "Virtual surgery for patients with nasal obstruction: Use of computational fluid dynamics (MeComLand®, Digbody® & Noseland®) to document objective flow parameters and optimise surgical results". In: *Acta Otorrinolaringol Esp* 69.3 (2018), pp. 125–133.

[6] H.K. Versteeg and W. Malalasekera. *An Introduction to Computational Fluid Dynamics: The Finite Volume Method*. Pearson Education Limited, 2007. ISBN: 9780131274983. URL: https://books.google.se/books?id=RvBZ-UMpGzIC.

[7] Johan Ronnås and Jakob Widebrant. "Nasal Obstruction - Diagnosis and Prediction using Computational Fluid Dynamics". MA thesis. Gothenburg, Sweden: Chalmers University of Technology, 2020. URL: https://hdl.handle.net/20.500.12380/300988.

[8] Giancarlo B. Cherobin, Richard L. Voegels, Fábio R. Pinna, Eloisa M. M. S. Gebrim, Ryan S. Bailey, and Guilherme J. M. Garcia. "Rhinomanometry Versus Computational Fluid Dynamics: Correlated, but Different Techniques". In: *American Journal of Rhinology & Allergy* 35.2 (2021). PMID: 32806938, pp. 245–255. DOI: 10.1177/1945892420950157. eprint: https://doi.org/10.1177/1945892420950157.

[9] Thomas Radulesco, Lionel Meister, Gilles Bouchet, Arthur Varoquaux, J. Giordano, Julien Mancini, Patrick Dessi, Pierre Perrier, and Justin Michel. "Correlations between Computational Fluid Dynamics and clinical evaluation of nasal airway obstruction due to septal deviation: an observational study". In: *Clinical Otolaryngology* 44 (Apr. 2019). DOI: 10.1111/coa.13344.

[10] Kai Zhao, Jianbo Jiang, Kara Blacker, Brian Lyman, Pamela Dalton, Beverly Cowart, and Edmund Pribitkin. "Regional Peak Mucosal Cooling Predicts the Perception of Nasal Patency". In: *The Laryngoscope* 124 (Mar. 2014). DOI: 10.1002/lary.24265.

[11] Eugene Wong and Ronald Eccles. "Comparison of the classic and Broms methods of rhinomanometry using model noses". In: *European archives of oto-rhino-laryngology : official journal of the European Federation of Oto-Rhino-Laryngological Societies (EUFOS) : affiliated with the German Society for Oto-Rhino-Laryngology - Head and Neck Surgery* 272 (May 2014). DOI: 10.1007/s00405-014-3083-6.

[12] Jong-Hoon Lee, Yang Na, Sung-Kyun Kim, and Seung-Kyu Chung. "Unsteady flow characteristics through a human nasal airway". In: *Respiratory Physiology Neurobiology* 172.3 (2010), pp. 136–146. ISSN: 1569-9048. DOI: https://doi.org/10.1016/j.resp.2010.05.010.

[13] Hojat Bahmanzadeh, Omid Abouali, and Goodarz Ahmadi. "Unsteady particle tracking of micro-particle deposition in the human nasal cavity under cyclic inspiratory flow". In: *Journal of Aerosol Science* 101 (2016), pp. 86–103. ISSN: 0021-8502. DOI: https://doi.org/10.1016/j.jaerosci.2016.07.010.

[14] Hadrien Calmet, Alberto M. Gambaruto, Alister J. Bates, Mariano Vázquez, Guillaume Houzeaux, and Denis J. Doorly. "Large-scale CFD simulations of the transitional and turbulent regime for the large human airways during rapid inhalation". In: *Computers in Biology and Medicine* 69 (2016), pp. 166–180. ISSN: 0010-4825. DOI: https://doi.org/10.1016/j.compbiomed.2015.12.003.

[15] E. Moreddu, L. Meister, C. Philip-Alliez, J.-M. Triglia, M. Medale, and R. Nicollas. "Computational Fluid Dynamics in the assessment of nasal obstruction in children". In: *European Annals of Otorhinolaryngology, Head and Neck Diseases* 136.2 (2019), pp. 87–92. ISSN: 1879-7296. DOI: https://doi.org/10.1016/j.anorl.2018.11.008.

[16] James Van Strien, Kendra Shrestha, Sargon Gabriel, Petros Lappas, David F. Fletcher, Narinder Singh, and Kiao Inthavong. "Pressure distribution and flow dynamics in a nasal airway using a scale resolving simulation". In: *Physics of Fluids* 33.1 (2021), p. 011907. DOI: 10.1063/5.0036095. eprint: https://doi.org/10.1063/5.0036095. URL: https://doi.org/10.1063/5.0036095.

[17] *Body Planes and Sections.* [Online; accessed 2021-06-23]. Aug. 14, 2020. URL: https://med.libretexts.org/@go/page/7289.

[18] Oliver Jones. *The Nasal Cavity.* Sept. 2019. URL: https://teachmeanatomy.info/head/organs/the-nose/nasal-cavity/.

[19] Wikimedia Commons. *File:Nose and nasal cavities.png — Wikimedia Commons, the free media repository.* [Online; accessed 10-August-2021]. 2020. URL:

https://commons.wikimedia.org/w/index.php?title=File:Nose_and_nasal_cavities.png&oldid=487737037.

[20] Munakomi S. Sobiesk JL. *Anatomy, Head and Neck, Nasal Cavity.* Treasure Island (FL): StatPearls Publishing. Jan. 2021. URL: https://www.ncbi.nlm.nih.gov/books/NBK544232/.

[21] Nick Jones. "The nose and paranasal sinuses physiology and anatomy". In: *Advanced Drug Delivery Reviews* 51.1 (2001). Nasal Vaccines, pp. 5–19. ISSN: 0169-409X.

[22] Kristin Hayes. *The Anatomy of the Nasal Cavity.* Medically reviewed by William Truswell, MD. 2021. URL: https://www.verywellhealth.com/nasal-cavity-anatomy-5097506.

[23] P. A. Clement. "Committee report on standardization of rhinomanometry". In: *Rhinology* 22.3 (Sept. 1984), pp. 151–155.

[24] P. A. Clement and F. Gordts. "Consensus report on acoustic rhinometry and rhinomanometry". In: *Rhinology* 43.3 (Sept. 2005), pp. 169–179.

[25] P Broms, Bjorn Jonson, and C Lamm. "Rhinomanometry. II. A system for numerical description of nasal airway resistance". In: *Acta oto-laryngologica* 94 (July 1982), pp. 157–68. DOI: 10.3109/00016488209128900.

[26] Howard H. Hu. "Chapter 10 - Computational Fluid Dynamics". In: *Fluid Mechanics (Fifth Edition).* Ed. by Pijush K. Kundu, Ira M. Cohen, and David R. Dowling. Fifth Edition. Boston: Academic Press, 2012, pp. 421–472. ISBN: 978-0-12-382100-3. DOI: https://doi.org/10.1016/B978-0-12-382100-3.10010-1. URL: https://www.sciencedirect.com/science/article/pii/B9780123821003100101.

[27] Davidson L. *Fluid mechanics, turbulent flow and turbulence modeling.* Chalmers University of Technology, 2019.

[28] Zhe Zheng, Hong Liu, Qi Xu, Wei Wu, Liling Du, Hong Chen, Yiwen Zhang, and Dongxu Liu. "Computational fluid dynamics simulation of the upper airway response to large incisor retraction in adult class I bimaxillary protrusion patients". In: *Scientific Reports* 7 (2017).

[29] C. Li, J. Jiang, H. Dong, and K. Zhao. "Computational modeling and validation of human nasal airflow under various breathing conditions". In: *J Biomech* 64 (Nov. 2017), pp. 59–68.

[30] D. Taylor, D. Doorly, and R. Schroter. "Inflow boundary profile prescription for numerical simulation of nasal airflow". In: *Journal of The Royal Society Interface* 7 (2009), pp. 515–527.

[31] Kiao Inthavong, Prashant Das, Narinder Singh, and Josué Sznitman. "In silico approaches to respiratory nasal flows: A review". In: *Journal of Biomechanics* 97 (2019), p. 109434. ISSN: 0021-9290. DOI: https://doi.org/10.1016/j.jbiomech.2019.109434. URL: https://www.sciencedirect.com/science/article/pii/S0021929019306815.

[32] H. Calmet, K. Inthavong, H. Owen, D. Dosimont, O. Lehmkuhl, G. Houzeaux, and M. Vázquez. "Computational modelling of nasal respiratory flow". In: *Comput Methods Biomech Biomed Engin* 24.4 (Mar. 2021), pp. 440–458.

[33] Hallett S, Toro F, and Ashurst JV. *Physiology, Tidal Volume.* Treasure Island (FL): StatPearls Publishing. Jan. 2021. URL: https://www.ncbi.nlm.nih.gov/books/NBK482502/.

[34] Kiao Inthavong, Annicka Chetty, Yidan Shang, and Jiyuan Tu. “Examining mesh independence for flow dynamics in the human nasal cavity”. In: *Computers in Biology and Medicine* 102 (2018), pp. 40–50. ISSN: 0010-4825. DOI: https://doi.org/10.1016/j.compbiomed.2018.09.010.

[35] D.J. Doorly, D.J. Taylor, and R.C. Schroter. “Mechanics of airflow in the human nasal airways”. In: *Respiratory Physiology Neurobiology* 163.1 (2008). Respiratory Biomechanics, pp. 100–110. ISSN: 1569-9048. DOI: https://doi.org/10.1016/j.resp.2008.07.027. URL: https://www.sciencedirect.com/science/article/pii/S1569904808002140.

[36] Jian Wen, Kiao Inthavong, Jiyuan Tu, and Simin Wang. “Numerical simulations for detailed airflow dynamics in a human nasal cavity”. In: *Respiratory physiology amp; neurobiology* 161.2 (Apr. 2008), pp. 125–135. ISSN: 1569-9048. DOI: 10.1016/j.resp.2008.01.012. URL: https://doi.org/10.1016/j.resp.2008.01.012.

[37] H. Shi, C. Kleinstreuer, and Z. Zhang. “Laminar airflow and nanoparticle or vapor deposition in a human nasal cavity model”. In: *J Biomech Eng* 128.5 (Oct. 2006), pp. 697–706.

[38] D. Isabey and H. K. Chang. “Steady and unsteady pressure-flow relationships in central airways”. In: *J Appl Physiol Respir Environ Exerc Physiol* 51.5 (Nov. 1981), pp. 1338–1348.

A

Appendix 1

A.1 Boundary condition - velocity

```
FoamFile
{
    version     2.0;
    format      binary;
    class       volVectorField;
    arch        "LSB;label=32;scalar=64";
    location    "0";
    object      U;
}
// * * * * * * * * * * * * * * * * * * * * * * * * * * * * * * *
    * * * * * * * * //

dimensions      [0 1 -1 0 0 0 0];


internalField   uniform (0 0 0);

boundaryField
{
    face
    {
        type            noSlip;
    }
    atmosphere
    {
        type            pressureInletOutletVelocity;
        value           uniform (0 0 0);
    }
    nasalcavity
    {
        type            noSlip;
    }
```

```
    throat
    {
        type            flowRateOutletVelocity;
        volumetricFlowRate
        {
            type                csvFile;
            nHeaderLine         0;
            refColumn           0;
            componentColumns    (1);
            separator           ",";
            mergeSeparators     no;
            file                "flowrate15BC.csv";
        }
        value           uniform (0 0 0);
    }
    wall
    {
        type            noSlip;
    }
}
// * * * * * * * * * * * * * * * * * * * * * * * * * * * * * *
    * * * * * * * * * //
```

A.2 Boundary condition - pressure

```
FoamFile
{
    version     2.0;
    format      binary;
    class       volScalarField;
    arch        "LSB;label=32;scalar=64";
    location    "0";
    object      p;
}
// * * * * * * * * * * * * * * * * * * * * * * * * * * * * * *
    * * * * * * * * * //

dimensions      [0 2 -2 0 0 0 0];


internalField   uniform 0;

boundaryField
{
    face
    {
```

```
        type                zeroGradient;
    }
    atmosphere
    {
        type                totalPressure;
        rho                 rho;
        psi                 none;
        gamma               1;
        p0                  uniform 0;
        value               uniform 0;
    }
    nasalcavity
    {
        type                zeroGradient;
    }
    throat
    {
        type                zeroGradient;
    }
    wall
    {
        type                zeroGradient;
    }
}

// * * * * * * * * * * * * * * * * * * * * * * * * * * * * *
    * * * * * * * * //
```

A.3 fvSchemes dictionary

```
FoamFile
{
    version         2.0;
    format          ascii;
    class           dictionary;
    location        "system";
    object          fvSchemes;
}
// * * * * * * * * * * * * * * * * * * * * * * * * * * * * *
    * * * * * * * * //

ddtSchemes
{
    default             backward;
}
```

```
gradSchemes
{
    default          cellLimited leastSquares 1;
}

divSchemes
{
    default          none;
    div(phi,U)       bounded Gauss linearUpwindV grad(U);
    div((nuEff*dev2(T(grad(U))))) Gauss linear;
}

laplacianSchemes
{
    default          Gauss linear corrected;
}

interpolationSchemes
{
    default          linear;
}

snGradSchemes
{
    default          corrected;
}

wallDist
{
    method meshWave;
}

// * * * * * * * * * * * * * * * * * * * * * * * * * * * * * * *
    * * * * * * * * //
```

A.4 fvSolution dictionary

```
FoamFile
{
    version     2.0;
    format      ascii;
    class       dictionary;
    location    "system";
    object      fvSolution;
}
```

```
// * * * * * * * * * * * * * * * * * * * * * * * * * * * * *
    * * * * * * * * //

solvers
{
    p
    {
        solver          GAMG;
        tolerance       1e-07;
        relTol          0.01;
        smoother        DICGaussSeidel;
    }

    pFinal
    {
        $p;
        relTol    0;
    }

    U
    {
        solver          smoothSolver;
        smoother        symGaussSeidel;
        tolerance       1e-06;
        relTol          0.1;
    }

    UFinal
    {
        $U;
        relTol    0;
    }
}

PIMPLE
{
    correctPhi              yes;
    nOuterCorrectors        50;
    nCorrectors             2;
    nNonOrthogonalCorrectors  2;

    consistent          yes;
    pRefCell                0;
    pRefValue               0;

    residualControl
```

```
    {
        U
        {
            tolerance       1e-3;
            relTol          0;
        }

        p
        {
            tolerance       1e-3;
            relTol          0;
        }
}

relaxationFactors
{
    fields
    {
        p                   0.7;
        pFinal              0.9;
    }

    equations
    {
        U                                       0.9;
        UFinal                                  0.95;
    }
}

// * * * * * * * * * * * * * * * * * * * * * * * * * * * * *
    * * * * * * * * * //
```

B

Appendix 2

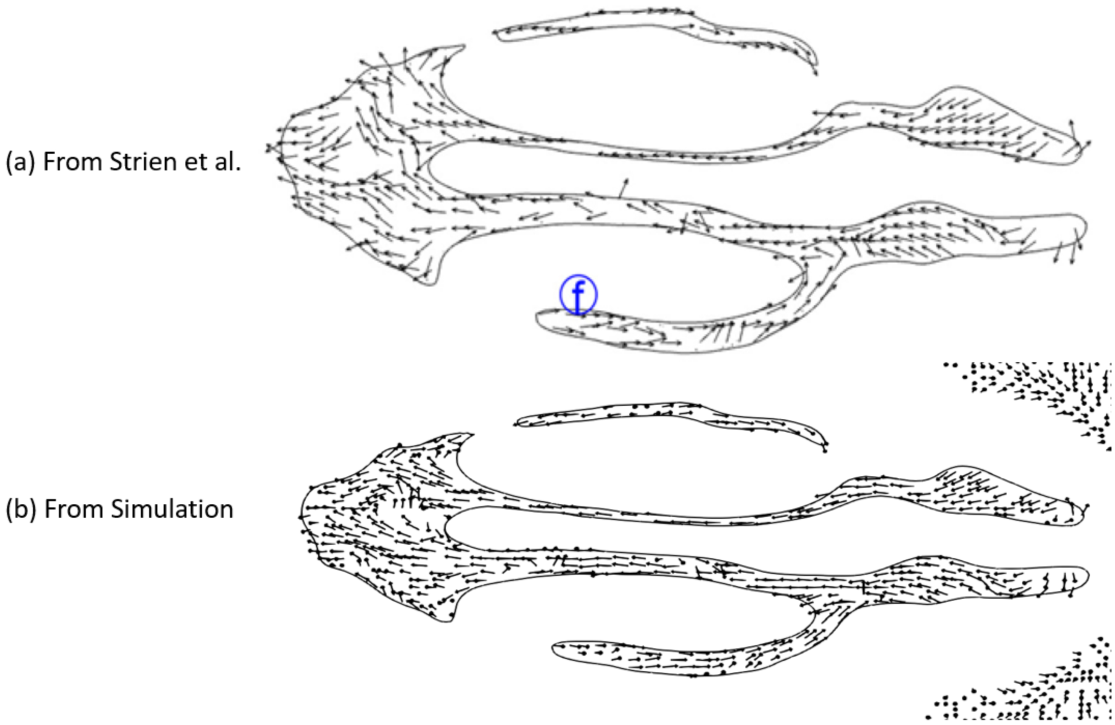

Figure B.1: Transverse plane - velocity vectors at time $t = 0.2$ seconds.

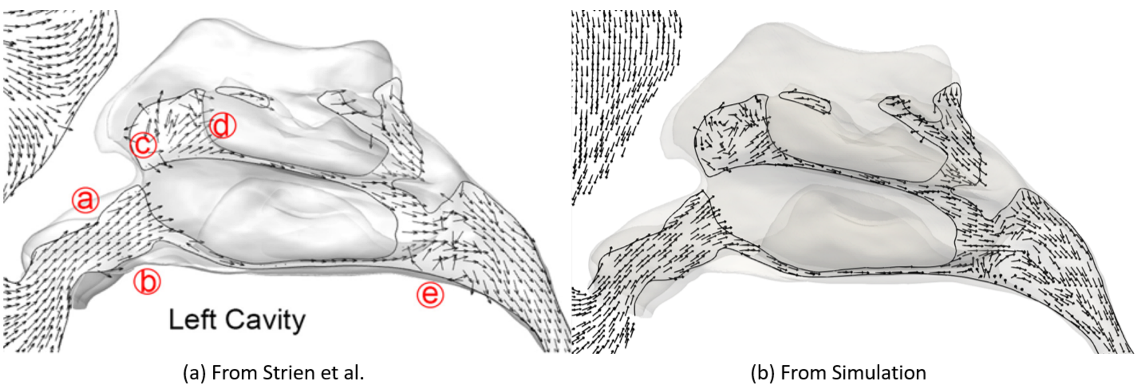

Figure B.2: Sagittal plane in left cavity - velocity vectors at time $t = 0.2$ seconds.

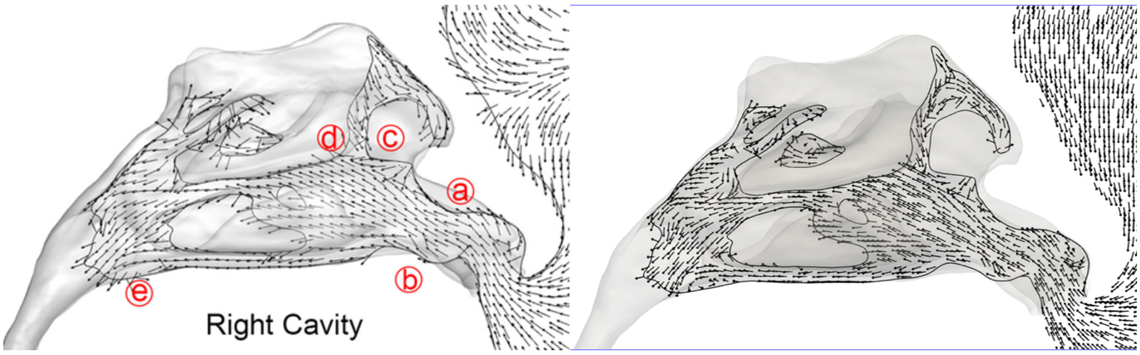

(a) From Strien et al.

(b) From Simulation

Figure B.3: Sagittal plane in right cavity - velocity vectors at time $t = 0.2$ seconds.

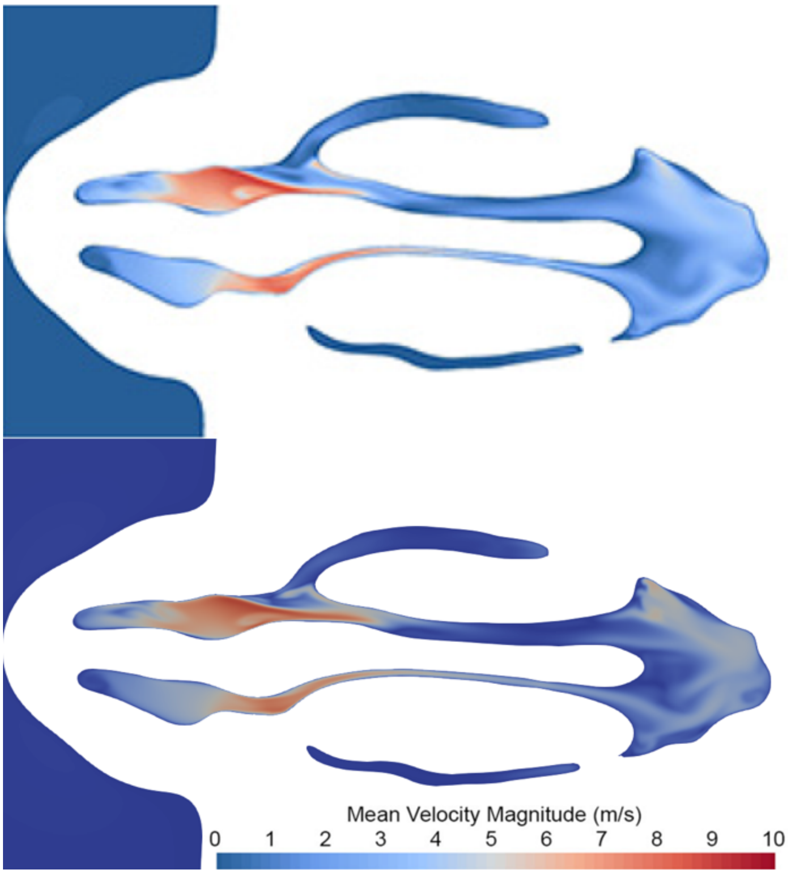

(a) From Strien et al.

(b) From Simulation

Figure B.4: Transverse plane - mean velocity contour.

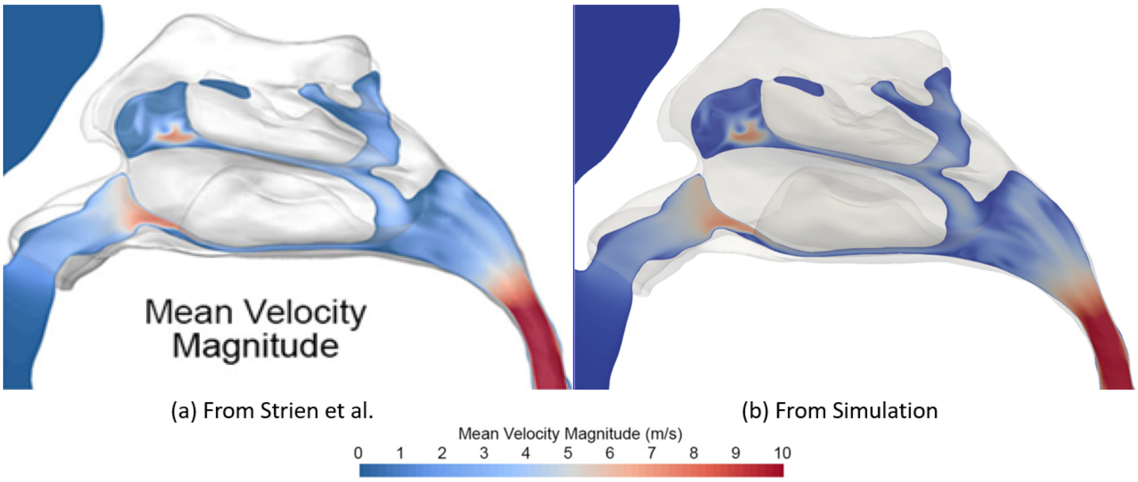

(a) From Strien et al. (b) From Simulation

Figure B.5: Sagittal plane in left cavity - mean velocity contour.

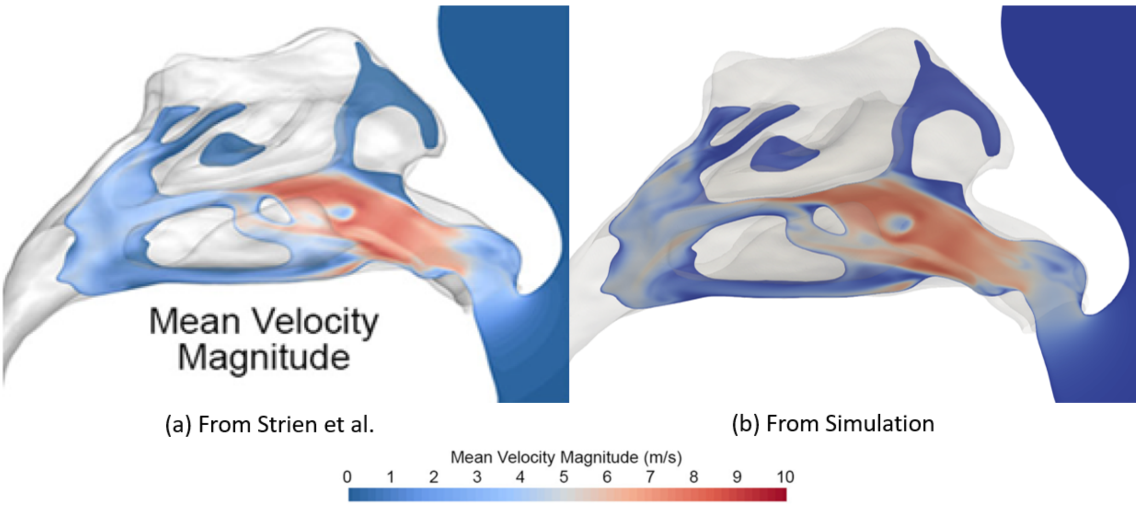

(a) From Strien et al. (b) From Simulation

Figure B.6: Sagittal plane in right cavity - mean velocity contour.

C

Appendix 3

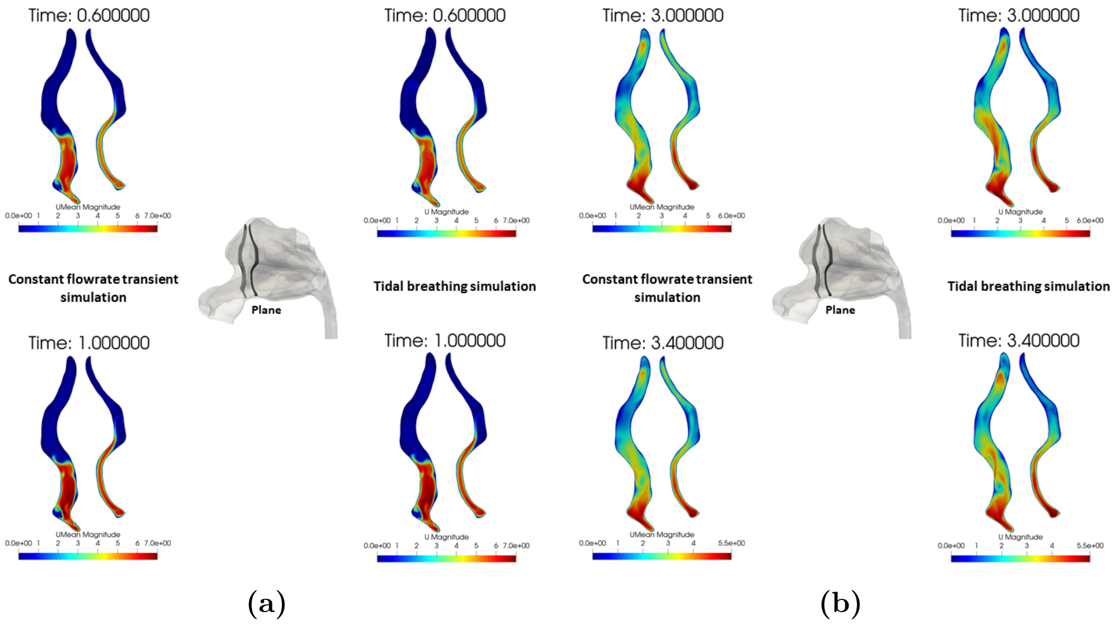

Figure C.1: Mean velocity contour at a coronal plane in anterior of the cavity.

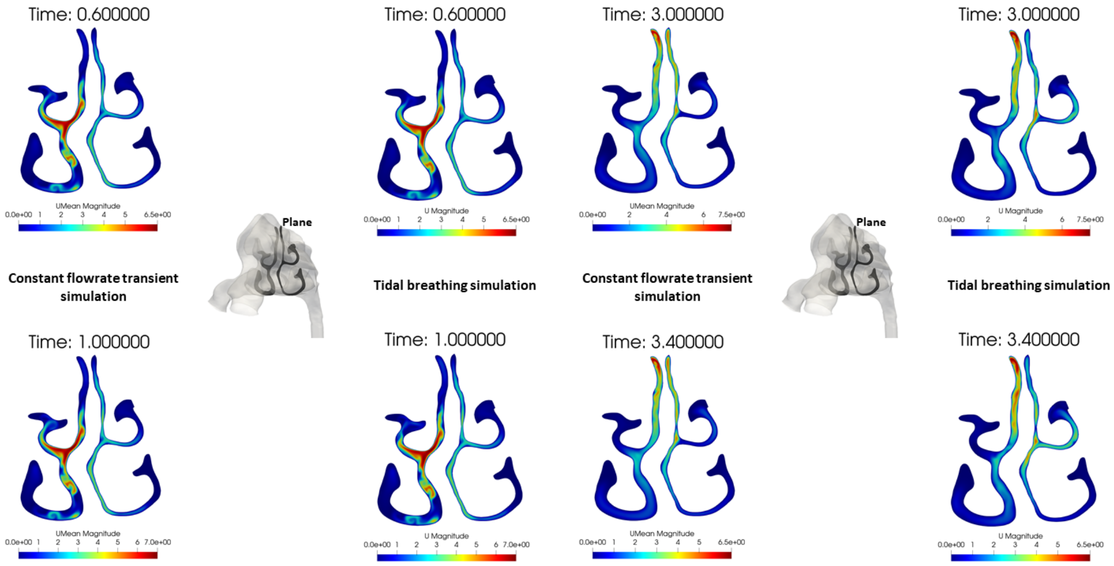

(a) (b)

Figure C.2: Mean velocity contour at a coronal plane in respiratory region.

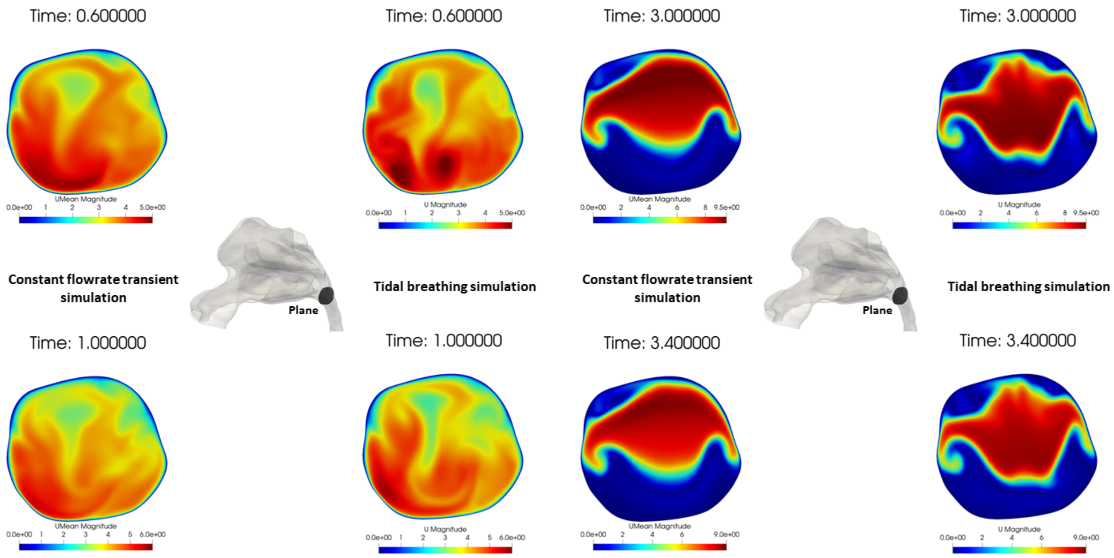

(a) (b)

Figure C.3: Mean velocity contour at a coronal plane in nasopharynx.

DEPARTMENT OF MECHANICS AND MARITIME SCIENCES
CHALMERS UNIVERSITY OF TECHNOLOGY
Gothenburg, Sweden
www.chalmers.se

CHALMERS
UNIVERSITY OF TECHNOLOGY